



Article

Geomorphology, Mineralogy, and Chronology of Mare Basalts in the Oceanus Procellarum Region

Cheng Zhang^{1,2}, Jianping Chen^{1,2,*}, Yiwen Pan^{1,2}, Shuangshuang Wu^{1,2}, Jian Chen³ , Xiaoxia Hu¹, Yue Pang^{1,2}, Xueting Liu^{1,2} and Ke Wang^{1,2}

¹ School of Earth Sciences and Resources, China University of Geosciences, Beijing 100083, China; 3001210074@email.cugb.edu.cn (C.Z.); panyw@email.cugb.edu.cn (Y.P.); 3001230099@email.cugb.edu.cn (S.W.); 2001210003@email.cugb.edu.cn (X.H.); 2101210001@email.cugb.edu.cn (Y.P.); 2012200012@email.cugb.edu.cn (X.L.); 2101220062@email.cugb.edu.cn (K.W.)

² Beijing Key Laboratory of Development and Research for Land Resources Information, Beijing 100083, China

³ Shandong Key Laboratory of Optical Astronomy and Solar-Terrestrial Environment, School of Space Science and Physics, Institute of Space Sciences, Shandong University, Weihai 264209, China; merchenj@mail.sdu.edu.cn

* Correspondence: 3s@cugb.edu.cn

Abstract: Mare basalts on the lunar surface are tangible expressions of the complex thermal evolution and geological processes that have occurred within the lunar interior. These basaltic manifestations are highly important because they provide invaluable insights into lunar geological evolution. Notably, the Oceanus Procellarum region, which is renowned for its extensive and long-lasting basaltic volcanism, is a premier location to investigate late-stage lunar thermal evolution. The primary aim of this research is to elucidate the geomorphological, compositional, and temporal attributes that define the mare basalts within the Oceanus Procellarum region. To achieve this aim, we comprehensively analyzed the geomorphological features present within the region, leveraging Kaguya/SELENE TC images and digital elevation models. Specifically, these geomorphological features encompass impact craters, wrinkle ridges, sinuous rilles, and volcanic domes. Subsequently, we thoroughly examined the mineralogical attributes of basalts in the Oceanus Procellarum region, leveraging Kaguya/SELENE MI data and compositional map products. To more accurately reflect the actual ages of the mare basalts in the Oceanus Procellarum region, we carefully delineated the geological units within the area and employed the latest crater size-frequency distribution (CSFD) technique to precisely determine their ages. This refined approach allowed for a more comprehensive and accurate understanding of the basaltic rocks in the study area. Overall, our comprehensive study included an in-depth analysis of the volcanic activity and evolution of the Oceanus Procellarum region, along with an examination of the correlation between the mineralogical composition and ages of mare basalts. The findings from this exhaustive investigation reveal a definitive age range for basalt units within the Oceanus Procellarum region from approximately 3.69 Ga to 1.17 Ga. Moreover, the latest mare basalts that formed were pinpointed north of the Aristarchus crater. Significantly, the region has experienced at least five distinct volcanic events, occurring approximately 3.40 Ga, 2.92 Ga, 2.39 Ga, 2.07 Ga, and 1.43 Ga, leading to the formation of multiple basalt units characterized by their unique mineral compositions and elemental abundances. Through the application of remote sensing mineralogical analysis, three primary basalt types were identified: low-titanium, very-low-titanium, and intermediate-titanium basalt. Notably, the younger basalt units exhibit an elevated titanium proportion, indicative of progressive olivine enrichment. Consequently, these younger basalt units exhibit more intricate and complex mineral compositions, offering valuable insights into the dynamic geological processes shaping the lunar surface.

Keywords: mare basalts; Oceanus Procellarum; geomorphology; mineralogy; crater size-frequency distribution (CSFD)



Citation: Zhang, C.; Chen, J.; Pan, Y.; Wu, S.; Chen, J.; Hu, X.; Pang, Y.; Liu, X.; Wang, K. Geomorphology, Mineralogy, and Chronology of Mare Basalts in the Oceanus Procellarum Region. *Remote Sens.* **2024**, *16*, 634. <https://doi.org/10.3390/rs16040634>

Academic Editor: Jonathan H. Jiang

Received: 17 December 2023

Revised: 25 January 2024

Accepted: 4 February 2024

Published: 8 February 2024



Copyright: © 2024 by the authors. Licensee MDPI, Basel, Switzerland. This article is an open access article distributed under the terms and conditions of the Creative Commons Attribution (CC BY) license (<https://creativecommons.org/licenses/by/4.0/>).

1. Introduction

Lunar geological evolution represents a pivotal scientific goal within the realm of lunar exploration [1]. Mare basalts, which envelop approximately 17% of the lunar surface, play a central role in this pursuit [2]. Accurately determining the ages of mare basalts is highly important because it facilitates a more profound understanding of lunar volcanic activity and thermal evolution [3,4]. Of particular significance, the Oceanus Procellarum region is assumed to play a central role as the epicenter of the most extensive and long-lasting occurrences of late-stage mare basaltic volcanism on the lunar surface. Consequently, this area is the foremost location for in-depth exploration of the Moon's late-stage thermal evolution [5].

The lunar sample return missions of the Luna and Apollo programs brought back approximately 382 kg of lunar rock and soil specimens. Through rigorous isotopic analyses, the ages of mare basalts and pyroclastic glasses have been precisely determined to be within the range of approximately 3.1 Ga to ~3.9 Ga [6–8]. These findings provide indispensable reference points for the comprehensive examination of the Moon's volcanic history and thermal evolutionary processes [7,9]. In 2020, 1731 g of lunar sample was successfully returned by Chang'e-5 (CE-5) mission, China's maiden sample return mission [10]. The isotopic age analyses of these lunar samples reveal an approximate age of ~2.03 Ga, facilitating a fresh comprehension of late-stage lunar volcanism [10–12]. However, it is worth noting that precise age determinations for mare basalts are currently limited to a few sample locations. Age determination of global mare basalts relies heavily on remote sensing techniques, such as crater counting, a method that has been widely studied and includes methods such as those of Hartmann (1966) [13], Neukum et al. (1971) [14], Hartmann (1984) [15], Hiesinger et al. (2012) [16], and Yue et al. (2022) [17]. There is a substantial ongoing debate regarding the cessation of late-stage lunar volcanic activity. The prevailing view is that lunar mare volcanic activity on the near side of the Moon commenced at approximately 4.0 Ga and ceased before 2.5 Ga, with a total duration of approximately 1.5 Ga [18–23]. However, in 2011, Morota et al. conducted CSFD measurements on the Procellarum KREEP Terrane (PKT) and proposed that lunar volcanic activity persisted until approximately 1.5 Ga [4]. However, Hiesinger et al. (2003) [5], using a dating method of CSFD based on remote sensing data, suggested that lunar volcanic activity may have persisted until approximately 1 Ga. Braden et al. (2014) [24], through age determination of small irregular mare basalt patches on the lunar nearside, proposed that their formation occurred at approximately 100 Ma, which is notably younger than the previously determined cessation of volcanic activity, as indicated by Hiesinger et al. (2011) [25].

Oceanus Procellarum, the largest mare basalt region on the Moon's surface, has experienced multiple large-scale volcanic eruptions and basaltic infillings [3]. It is characterized by high abundances of heat-producing elements, such as thorium, potassium, and uranium [26–30], as well as low elevations and thin crust [31,32]. To date, numerous scholars have conducted extensive studies on various aspects of the Procellarum region, including the composition, thickness, and geological features of mare basalts [27,33–41]. These studies provide valuable references for a deeper understanding of mare basalts in the Procellarum region, aiding in the identification of essential details of lunar geological evolution. Previous research has included extensive remote sensing dating work on mare basalts in the Oceanus Procellarum region. Boyce et al. (1974) [42] and Boyce (1976) [43] used crater morphology methods to establish a model age of 2.5 Ga for Oceanus Procellarum, considering Aristarchus as the youngest area, with a model age of 1.7 Ga. Young (1977) [44] conducted CSFD measurements in the northern part of Oceanus Procellarum, suggesting that lunar mare volcanic activity may have persisted until ~1.97 Ga to ~1.57 Ga. Schultz and Spudis (1983) [45] proposed that basalts surrounding the Lichtenberg crater in the middle of Oceanus Procellarum are younger than 1 Ga. Hiesinger et al. (1998; 2001; 2002; 2003; 2010; 2011) [5,18,19,25,46–48] classified mare basalt units using Clementine data and determined mare basalt ages through CSFD measurements. In the Oceanus Procellarum region, mare basalts have been determined to have ages ranging from ~3.7 Ga to ~1.2 Ga,

with the youngest mare basalts located around the Aristarchus plateau, considering the Oceanus Procellarum and Mare Imbrium regions as the youngest areas [5]. Morota et al. (2011) [4] conducted comprehensive dating of 49 young mare basalt units in the Oceanus Procellarum region using both the Neukum chronology model [49] and the Ivanov chronology model [50], suggesting that lunar volcanic activity persisted until ~1.5 Ga, possibly peaking at approximately 2.2 Ga to 1.8 Ga, with the youngest mare basalt units appearing in the central area of the Procellarum KREEP Terrane (PKT). Chen et al. (2022) [51] published a 1:2.5 million lunar lithologic map. The ages of mare basalt units in the Oceanus Procellarum region were determined to be between 3.7 Ga and 1.7 Ga, which is largely based on the units and mode ages of Hiesinger et al. (2003) [5], with supplements of new CSFD dating results on some previously unidentified basalt areas from Morota et al. (2011) [4]. Following the successful implementation of the CE-5 mission, many scholars have conducted chronological investigations in the region of the landing area in the Oceanus Procellarum. However, the results from different studies have shown variations [52–57]. Zhao et al. (2023) [3] conducted a geochronological study of mare basalts at the boundaries of lunar maria, including the Oceanus Procellarum, Mare Imbrium, Mare Vaporum, and Mare Insularum regions. Mare basalts with model ages ranging from 3.78 Ga to 1.71 Ga were obtained, with the estimation that the last major eruption occurred at approximately 1.8 Ga.

This study, based on various high-resolution data from multiple sources and the latest research findings from CE-5 mission samples, comprehensively explores the geomorphological characteristics, chemical compositions, mineralogical features, and evolution of mare basalts in the Procellarum region. We identified and extracted typical structural features in the Oceanus Procellarum region, including impact craters, sinuous rilles, wrinkle ridges, and dome structures, allowing for a systematic depiction of the detailed geological context of the Procellarum region. Furthermore, we performed a detailed classification of mare basalt units in the Oceanus Procellarum region based on new multisource data and obtained accurate model ages for the mare basalts using the latest dating model [17]. This enabled us to investigate the eruptive episodes of mare basalts and late-stage lunar volcanic activity. Finally, we explored the correlation between the age of mare basalts in the Oceanus Procellarum region and their composition and mineral content. Through this research, we provide crucial data and insights for a deeper understanding of mare basalts in the Procellarum region.

2. Datasets and Methods

2.1. Datasets

This study comprehensively investigated the Oceanus Procellarum region, focusing on its morphological, topographical, compositional, and chronological characteristics using high-resolution imaging and spectral datasets. We utilized Kaguya/SELENE TC image data (10 m/pixel) [58,59], topographic data synthesized from the Lunar Reconnaissance Orbiter (LRO) mission's Lunar Orbiter Laser Altimeter (LOLA) and Kaguya TC digital terrain model (DTM) (SLDEM2015, 59 m/pixel) [58] and a Lunar Reconnaissance Orbiter Camera (LROC) (Narrow Angle Camera (NAC, 0.25–2 m/pixel) [60]) to describe the geological features of the Oceanus Procellarum region and extract small impact craters within it. Additionally, we employed FeO, CaO, Al₂O₃, MgO, TiO₂, and Mg# abundance maps derived from Kaguya/SELENE MI data (20 m/pixel) [61], along with Kaguya/SELENE MI false-color composites. Furthermore, semiglobal mineral abundance maps derived from Kaguya/SELENE MI data [62,63] were utilized to analyze the mineralogical variations in the Oceanus Procellarum region.

2.2. Compositional and Mineralogical Analyses

Otake et al. (2012) [64] developed an inversion algorithm to estimate FeO and TiO₂ contents using Kaguya/SELENE MI data and the method proposed by Lucey et al. (1998) [65]. Lemelin et al. (2015) [63] introduced a new algorithm for the inversion of FeO content using Kaguya/SELENE MI data and utilizing the Hapke radiative transfer model. The abundance

maps of FeO, CaO, Al₂O₃, MgO, TiO₂, and Mg# used in this study were derived from Wang et al. (2021) [66], who utilized machine learning algorithms to process Kaguya/SELENE MI data and generate chemical maps of the lunar surface.

Furthermore, we employed abundance maps of olivine, clinopyroxene, orthopyroxene, and plagioclase derived from Kaguya/SELENE MI data graciously supplied by Lemelin et al. (2019) [63]. The mare basalts are overlaid with numerous small and loosely packed regolith layers, which are primarily formed by fresh impact crater ejecta or subjected to intense space weathering processes [3]. To mitigate the effects of space weathering and gain deeper insight into the mineralogical variations among basaltic geological units, this study selected 6800 impact craters with diameters smaller than 1000 m for a comprehensive compositional and mineralogical analysis of basaltic geological units spanning different ages.

2.3. Topographical and Geochronological Analyses

Kaguya/SELENE TC image data and the SLDEM 2015 digital elevation model have been extensively utilized in studies of regional topography and local features [58,59]. Additionally, owing to their relatively high spatial resolution, Narrow Angle Camera (NAC) images are well suited for in-depth examination of small-scale geological features [60].

The determination of mare basalt ages typically involves multiple steps, including mare basalt unit classification, the selection of dating regions, the identification of impact craters, the removal of secondary craters, the determination of the area and crater diameter, and the application of dating models to generate CSFD curves and absolute model ages [3,67–69]. Mare basalts represent a ubiquitous lithological occurrence across the lunar surface, and their classification predominantly relies on the geological features and chemical composition of these rocks. Variances in material composition and content are frequently observed among mare basalts spanning different epochs. Consequently, researchers routinely employ criteria such as disparities in luminosity, morphological attributes, impact crater density, crater degradation level, spectral characteristics, and stratigraphic relationships to systematically categorize mare basalts [4].

Hiesinger et al. (1998; 2001; 2002; 2003; 2010; 2011) [5,18,19,25,46–48] and Morota et al. (2011) [4] have harnessed multispectral image datasets acquired from Clementine to delineate mare basaltic units within the tempestuous Oceanus Procellarum region. Nonetheless, owing to the comparatively reduced resolution of Clementine data, subtle distinctions may evade comprehensive discernment. In this study, we employed element abundance maps and false-color composites derived from the Multiband Imager (MI) data of Kaguya/SELENE, which has a spatial resolution of 20 m [66]. These data were used to delineate the boundaries of mare basalts in the Oceanus Procellarum region. False-color composites are highly sensitive to lunar soil maturity and composition [70]. We applied Kaguya/SELENE MI data in the visible wavelength range to generate ratio-based false-color composites, with the red channel (750 nm/415 nm) and green channel (750 nm/950 nm) reflecting variations in the lunar soil maturity and titanium content, respectively, while the blue channel (415 nm/750 nm) indicates changes in the iron content [70]. Furthermore, the selection of regions for chronological analysis must adhere to two pivotal prerequisites: (1) the designated area should exhibit relatively even terrain to minimize potential inaccuracies in crater diameter data resulting from substantial topographic undulations; (2) the chosen region should lack secondary impact craters, as these could exert direct influence on CSFD outcomes, potentially leading to a marginal inflation of estimated ages [71].

The CSFD is a prevalent method employed for estimating the absolute model age (AMA) of lunar surfaces and other planetary bodies [72]. This method is based on radioisotopic age data from lunar samples and involves the establishment of a function to infer the ages of planetary surface units. Simultaneously, this method is underpinned by two primary principles: (1) presuming a stochastic distribution of impact craters on the lunar surface within the same geological epoch; (2) maintaining a consistent pattern of

size-frequency relationships for impact craters across distinct geological epochs. Hartmann and several other researchers have made multiple improvements and optimizations to the CSFD curves [13,17,67,73,74]. Equation (1) [13,17,67,73,74] symbolizes the Neukum chronology model [49], acknowledged widely as a classical model. Equation (2) [17] symbolizes the revised chronology model proposed by Yue et al. (2022) [17], integrating the most recent research findings and updated ages of Chang'e-5 samples. Importantly, the modified ages for specific lunar regions reveal noteworthy disparities when juxtaposed with the ages predicted by the Neukum model [49].

$$N(1, t) = 5.44 \times 10^{-14}(e^{6.93t} - 1) + 8.38 \times 10^{-4}t \quad (1)$$

$$N(1, t) = 1.089 \times 10^{-13}(e^{6.757t} - 1) + 7.660 \times 10^{-4}t \quad (2)$$

In Equations (1) and (2), $N(1)$ represents the temporal variation of cumulative impact crater frequency at $D = 1$ km (number per km^2) over time (t), where t denotes the age (10^9 a).

In this study, we employed the CraterTools component [75] to extract impact craters with diameters exceeding 200 m and subsequently export. scc (space crater count) files. To ensure the efficacy and precision of the identified crater count, a rigorous validation process was undertaken by multiple assessors, culminating in meticulous reviews and requisite adjustments to the extraction results. Then, with craterstats2.sav software [68], we applied Yue et al.'s (2022) [17] updated dating model to determine the ages of mare basalt units in the Oceanus Procellarum region.

3. Results

3.1. Geomorphology

3.1.1. Impact Craters

In the Oceanus Procellarum region, there are numerous bowl-shaped and flat-floored craters, which tend to have relatively small diameters. The Galilaei T crater exhibits a representative bowl-shaped morphology in the region, showcasing a well-defined circular shape. False-color images of the crater materials exhibit significant differences from those of the surrounding terrain, indicating variations in elemental and mineral abundances (Figure 1a). Whereas The Guess crater exemplifies a typical flat-floored morphology on the Moon (Figure 1b). Within this area, there are also several impact craters that have been partially or completely inundated by late-stage mare basalts, resulting in the filling of crater floors and some parts of their walls. Notably, only some of the higher rim regions of these craters have remained uncovered. Typical impact craters inundated by mare basalts in this region include the Russell crater, with a diameter of 103 km; the Struve crater, with a diameter of 164 km; and the Eddington crater, with a diameter of 120 km (Figure 1c). Among them, the Struve crater is the largest crater in the area; its crater floor is filled by mare basalts, and it also contains many smaller impact craters that formed later. The Aristarchus crater stands out as one of the most prominent and brightest impact craters on the Moon and is characterized by its prominent rays (Figure 1d). Moreover, the central peak of Aristarchus is predominantly composed of feldspar supplemented by small quantities of pyroxene and olivine [76]. This composition suggests that Aristarchus may have unearthed a feldspar-rich crust during its formation [76,77]. The Lichtenberg crater exhibits typical radial rays, indicating that the impact direction for Lichtenberg was from the southeast (Figure 1e). The Briggs crater's floor features several irregular fractures of varying sizes, which are arranged in concentric, radial, or polygonal patterns, representing typical geological features of crater floors (Figure 1f).

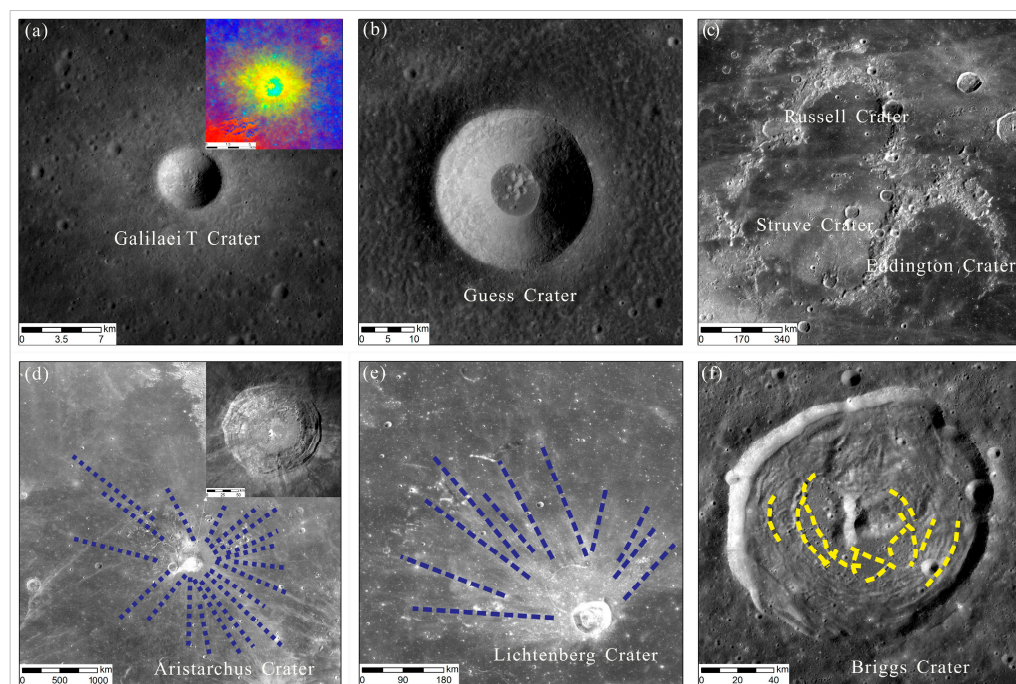


Figure 1. Representative impact craters in the Oceanus Procellarum region based on Kaguya/SELENE TC image. (a) A representative bowl-shaped crater in the area: Galilaei T crater. (b) A typical flat-floored crater in the region: Guess crater. (c) Representative craters inundated by mare basalts in the area: Russell crater, Struve crater, and Eddington crater. (d) An impact crater with the most prominent lunar rays: Aristarchus crater. The crater's rays are indicated by blue dashed lines. (e) An impact crater in the region exhibiting only one-sided lunar rays: Lichtenberg crater. The crater's rays are represented by blue dashed lines. (f) An impact crater in the region with typical crater floor fractures: Briggs crater. Typical crater floor fractures within the crater are depicted by yellow dashed lines.

3.1.2. Wrinkle Ridges

Wrinkle ridges are linear surface features extending across the lunar landscape. These features, distinguished by their elongated structure and relatively elevated positions, are primarily situated within and along the boundaries of mare basalt regions [78–80]. These geological features typically consist of gentle and wide-arched segments as well as sharp, irregular ridges [81,82]. Wrinkle ridge formation has been widely attributed to compressional stress forces in previous studies [78–80,83], with the formation spanning approximately 4 Ga to 1.2 Ga and peaking at approximately 3.5 Ga to 3.1 Ga [84,85]. Nypaver et al. (2022) [86] argue that the most recently active wrinkle ridges (approximately 1.5 Ga to 0.056 Ga) exhibit a slender and meandering morphology and are widely distributed within lunar nearside basalt. The formation of these ridges is believed to result from a combination of stresses induced by orbital, tidal, and crustal shrinkage and from impact events.

In the Oceanus Procellarum region, a total of 3898 wrinkle ridges have been systematically identified. Among these, the more distinctive formations include Wrinkle Ridge Bucher, Wrinkle Ridge Arduino, Wrinkle Ridge Argand, Wrinkle Ridge Niggli, Wrinkle Ridge Whiston, Wrinkle Ridge Scilla, Wrinkle Ridge Burnet, Wrinkle Ridge Ewing, and Wrinkle Ridge Rubey, while the remaining ridges remain unnamed. This comprehensive survey has significantly advanced our comprehension of the intricate and complex patterns shaping the wrinkle ridges within the Oceanus Procellarum region. Simultaneously, the analysis of the relationships between wrinkle ridges and mare basalt units serves as a valuable tool for determining the chronological sequence of basalt formation (Figure 2a).

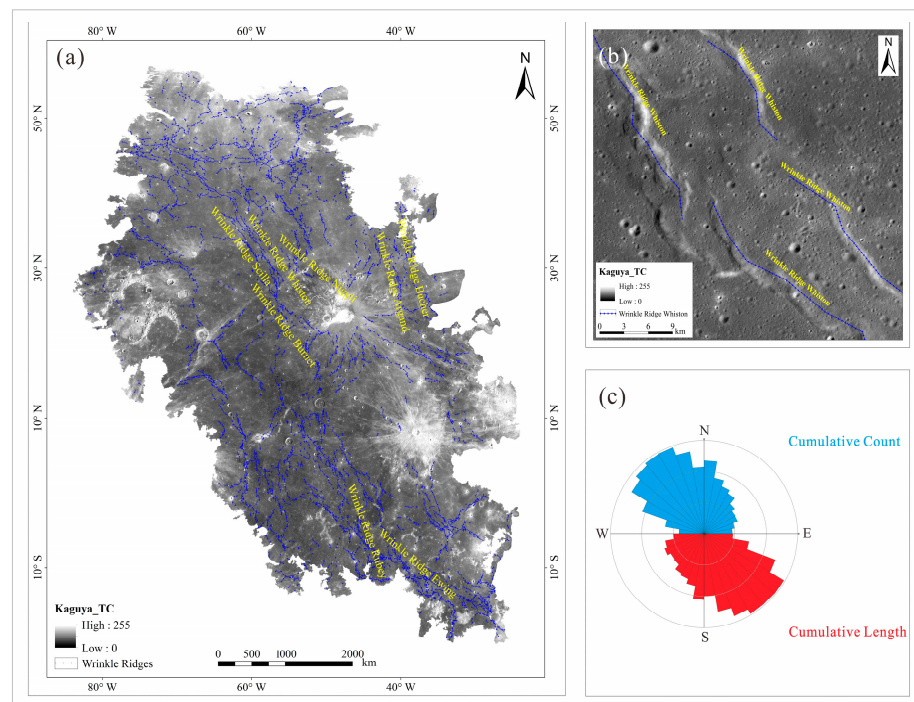


Figure 2. Wrinkle ridges in the Oceanus Procellarum Region. (a) Wrinkle ridges in the Oceanus Procellarum area. The blue lines represent the wrinkle ridge structures. (b) Typical wrinkle ridge: Dorsa Whiston. The blue lines represent the plot of the trend of Dorsa Whiston. (c) Rose diagram of wrinkle ridges in the Oceanus Procellarum area.

The Dorsa Whiston, located in the Oceanus Procellarum region, exemplifies a typical linear wrinkle ridge with an approximate length of 221 km, as depicted in Figure 2a. In comparison to other regions, the northwestern portion of the Oceanus Procellarum area features a greater density of linear wrinkle ridges [87], as shown in Figure 2b. This observation signifies the prevalent stress and magmatic activity in the area. An analysis of rose diagrams for ridge orientation-frequency and ridge orientation-length cumulations in the Oceanus Procellarum region reveals that the majority of the wrinkle ridges are primarily oriented in the NW–SE direction. Consequently, the formation of wrinkle ridges in the Oceanus Procellarum region is likely influenced primarily by compressional stress in the NE–SW direction. The rose diagrams for ridge orientation-frequency cumulation and ridge orientation-length cumulation in the area point in this direction, implying that the formation of wrinkle ridges in Oceanus Procellarum was primarily controlled by directional compressional stress (Figure 2c).

3.1.3. Sinuous Rilles

Sinuuous rilles are primarily distributed within mare basalt regions and appear as slender, meandering channels, often originating from circular or arcuate depressions and frequently accompanied by pyroclastic deposits [88,89]. The formation of lunar rilles signifies past volcanic eruptions in the area [90].

In the Oceanus Procellarum region, we have identified a total of 155 lunar rilles. Among these, the more prominent examples include Rima Sharp, Rima Brayley, Rima Diophantus, Rima Marius, Rima Galilaei, Rima Aristarchus, Rima Suess, Rima Milichius, and Rima Herigonius. Notably, the density of lunar rilles is relatively higher around the Aristarchus crater (Figure 3a). Rima Marius, a typical sinuous rille in the Oceanus Procellarum region, consists of two segments measuring 280 km and 212 km in length (Figure 3b). False-color composite imagery suggests that Rima Marius exhibits significant color variations compared to the surrounding mare basalts, implying a higher titanium (Ti) content, indicating a magma source with an elevated degree of evolution or lower partial

melting degree (Figure 3b). The Oceanus Procellarum region hosts several typical lunar rilles, which are more dense in the central area and often feature volcanic vents at their sources, such as Rimae Aristarchus, Rima Sharp [91], Rimae Prinz [90], Rimae Maestlin, and Rima Agricola (Figure 3c).

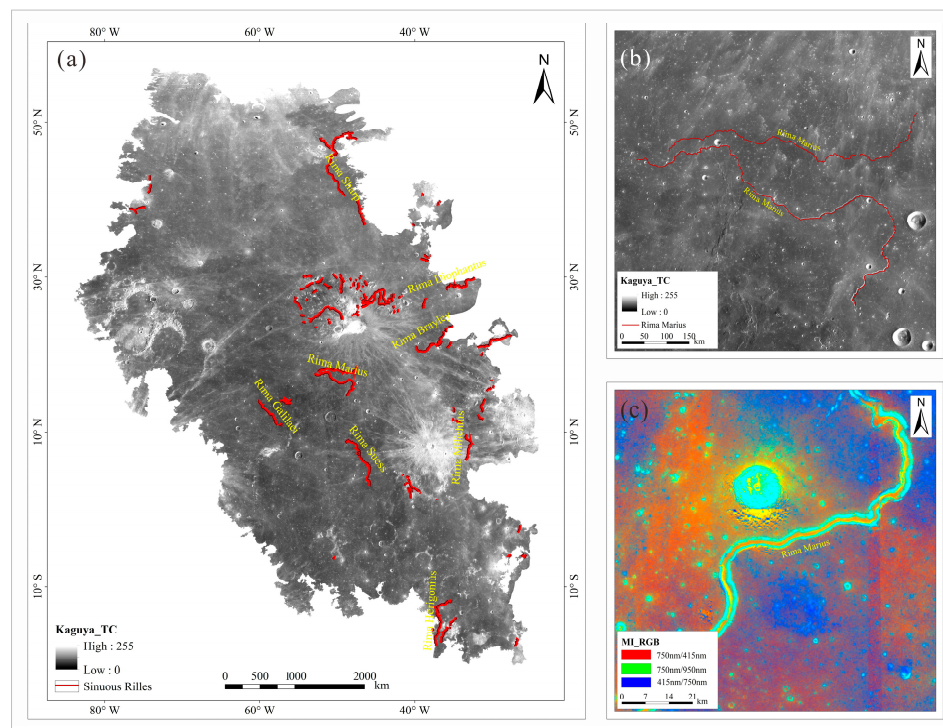


Figure 3. Sinuous rilles in the Oceanus Procellarum region. (a) Comprehensive map of lunar rilles within the Oceanus Procellarum region. (b) Depiction of a typical lunar rille in the area: Rima Marius. The blue lines represent the overall trend and trajectory of Rima Marius. (c) False-color composite image of Rima Marius.

3.1.4. Volcanic Domes

Volcanic domes are common broad, circular, or semicircular raised landforms in mare basalt areas and are primarily formed by the extrusion and intrusion of magma [92,93] (Figure 4d,e). In the Oceanus Procellarum region, an exhaustive examination has been conducted, leading to the identification of a total of 17 expansive volcanic domes. Notable among them are the Aristarchus Plateau, Helmet, Marius Hill, Mons Gruithuisen Delta, Mons Rümker, and Prinz–Harbinger. It is pertinent to highlight that each of these substantial volcanic domes frequently harbors numerous smaller volcanic domes (Figure 4a). The Oceanus Procellarum region hosts numerous volcanic dome structures, with Marius Hill exhibiting the highest density, thereby indicating complex volcanic activity in this area [94]. A total of 87 volcanic domes are identified within Marius Hill (Figure 4b). The false-color composite image exhibits complex mixed hues, suggesting a diverse composition in the region, featuring a higher olivine content compared to that in other areas (Figure 4c). Volcanic domes are also widespread in several typical subregions of the Oceanus Procellarum region, including the Mons Gruithuisen Delta, Mons Gruithuisen Gamma, Mons Hansteen, Aristarchus Plateau, and Mons Rümker [56,95].

3.2. Age of the Mare Basalts

Hiesinger et al. (2003) [5] utilized color variations in Clementine data to partition lunar mare basalt units in the Oceanus Procellarum region into 58 units, subsequently determining model ages for these basaltic formations. In this investigation, we build upon the mare basalt boundary delineation results reported by Hiesinger et al. (2003) [5] and reclassify them utilizing high-resolution Kaguya/SELENE MI elemental maps and

multispectral false-color composites. The modifications made aim to enhance clarity and precision in conveying the process of reclassification and the datasets employed. We divided the mare basalts in the Oceanus Procellarum region into 100 units (Figure 5). Within these 100 mare basalt units, we selected 167 areas that were flat and free from secondary impact crater interference. In these selected areas, we identified and mapped 25,835 craters with diameters exceeding 200 m. We recalculated the absolute model ages of the mare basalt units using the latest CSFD model [17], as shown in Table 1.

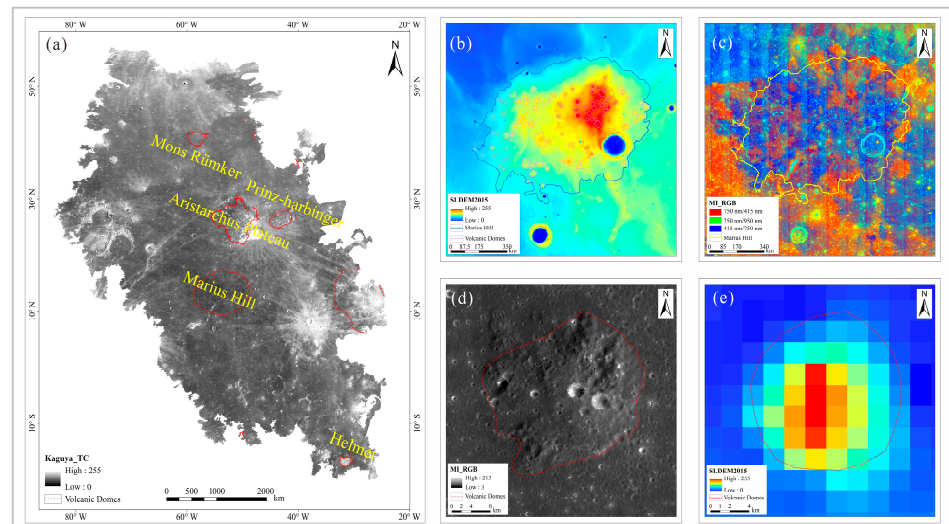


Figure 4. Volcanic domes in the Oceanus Procellarum region. (a) Comprehensive map of volcanic domes within the Oceanus Procellarum region. (b) Depiction of the summits of volcanic domes within Marius Hill. The yellow outline denotes the perimeter of Marius Hill, and the red lines signify the locations of the volcanic domes. (c) False-color composite image of Marius Hill. (d,e) Exemplification of a typical volcanic dome located on Marius Hill.

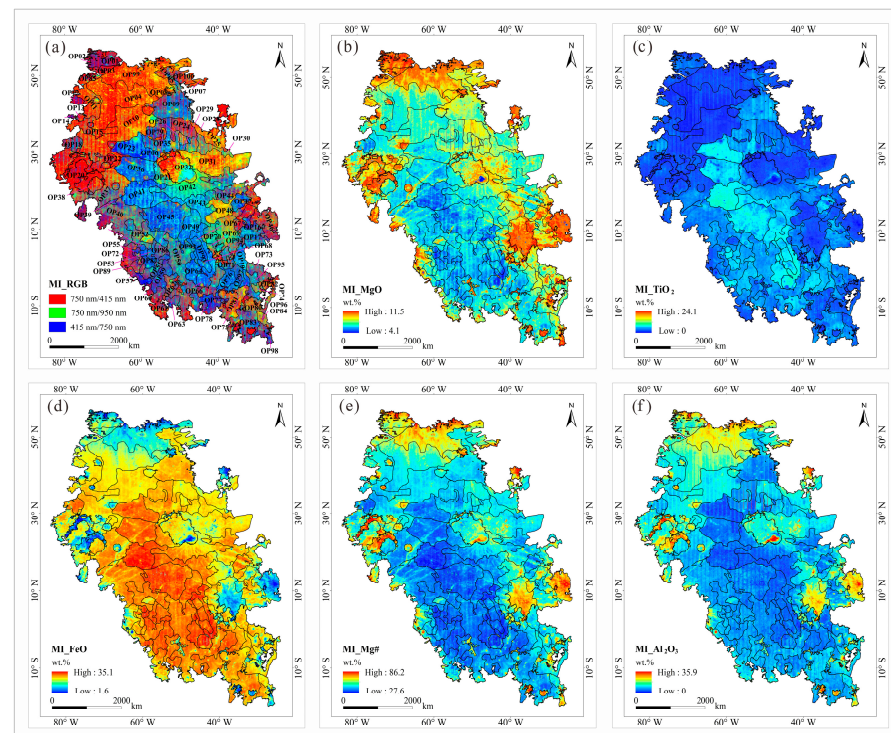


Figure 5. Map illustrating the division of mare basalt units. (a) MI false-color composite, (b) MgO abundance, (c) TiO₂ abundance, (d) FeO abundance, (e) Mg#, and (f) Al₂O₃ abundance.

Table 1. Model ages of lunar basaltic units in the Oceanus Procellarum region.

Unit	Hiesinger et al. (2011) [25]	Chen et al. (2022) [51]	Morota et al. (2011) Model A [4]	Morota et al. (2011) Model B [4]	Model Ages in This Study	Mean Model Ages in This Study
OP01	3.6 Ga	3.6 Ga	-	-	$3.63^{+0.021}_{-0.024}$ Ga $3.64^{+0.031}_{-0.039}$ Ga	3.63 Ga
OP02	3.6 Ga	3.6 Ga	-	-	$3.61^{+0.051}_{-0.078}$ Ga	3.61 Ga
OP03	2.9 Ga	2.9 Ga	2.87/3.70 Ga	3.05/3.70 Ga	$3.58^{+0.037}_{-0.048}$ Ga	3.58 Ga
OP04	3.4 Ga	3.4 Ga			$2.90^{+0.15}_{-0.21}$ Ga	2.90 Ga
OP05	1.7 Ga	1.7 Ga	2.50 Ga	2.82 Ga	$2.21^{+0.24}_{-0.24}$ Ga	2.21 Ga
OP06	-	-	-	-	$3.37^{+0.073}_{-0.13}$ Ga	3.37 Ga
OP07	-	-	-	-	$1.92^{+0.33}_{-0.33}$ Ga	1.92 Ga
OP08	3.4 Ga	3.4 Ga	-	-	$3.55^{+0.037}_{-0.048}$ Ga $3.29^{+0.055}_{-0.079}$ Ga	3.34 Ga
OP09	1.3 Ga	1.3 Ga	1.91/3.46 Ga	2.20/3.46 Ga	$2.06^{+0.11}_{-0.11}$ Ga	2.06 Ga
OP10	3.5 Ga	3.5 Ga			$3.41^{+0.020}_{-0.023}$ Ga $3.38^{+0.073}_{-0.13}$ Ga	3.41 Ga
OP11	3.1 Ga	3.1 Ga			$3.25^{+0.056}_{-0.079}$ Ga	3.25 Ga
OP12		3.1 Ga			$3.62^{+0.038}_{-0.051}$ Ga $3.52^{+0.039}_{-0.053}$ Ga	3.56 Ga
OP13	3.6 Ga	3.6 Ga	3.04 Ga	3.15 Ga	$3.16^{+0.088}_{-0.14}$ Ga	3.61 Ga
OP14					$3.50^{+0.051}_{-0.077}$ Ga	3.50 Ga
OP15					$2.31^{+0.26}_{-0.26}$ Ga $2.30^{+0.19}_{-0.20}$ Ga	2.30 Ga
OP16		3.3 Ga			$3.42^{+0.036}_{-0.047}$ Ga	3.42 Ga
OP17		3.0 Ga			$3.43^{+0.046}_{-0.064}$ Ga	3.43 Ga
OP18					$2.08^{+0.16}_{-0.16}$ Ga	2.08 Ga
OP19		1.9 Ga	2.20 Ga	2.53 Ga	$1.82^{+0.20}_{-0.20}$ Ga	1.82 Ga
OP20					$3.52^{+0.064}_{-0.11}$ Ga $3.35^{+0.048}_{-0.068}$ Ga $3.54^{+0.026}_{-0.032}$ Ga $3.42^{+0.061}_{-0.097}$ Ga $3.75^{+0.033}_{-0.042}$ Ga	3.47 Ga
OP21	1.2 Ga	1.2 Ga			$2.36^{+0.078}_{-0.078}$ Ga	2.43 Ga
OP22	2.9 Ga	2.9 Ga	3.31 Ga	3.32 Ga	$2.15^{+0.36}_{-0.36}$ Ga	2.15 Ga
OP23	1.7 Ga	1.7 Ga	2.10/3.52 Ga	2.43/3.48 Ga	$1.52^{+0.15}_{-0.15}$ Ga $1.42^{+0.14}_{-0.14}$ Ga	1.47 Ga
OP24	2.1 Ga	2.1 Ga	2.56 Ga	2.87 Ga	$2.90^{+0.082}_{-0.094}$ Ga	2.90 Ga
OP25		3.3 Ga			$3.33^{+0.084}_{-0.16}$ Ga $3.33^{+0.084}_{-0.16}$ Ga	3.32 Ga

Table 1. Cont.

Unit	Hiesinger et al. (2011) [25]	Chen et al. (2022) [51]	Morota et al. (2011) Model A [4]	Morota et al. (2011) Model B [4]	Model Ages in This Study	Mean Model Ages in This Study
OP26	2.9 Ga	2.9 Ga	3.21/3.49/3.72 Ga	3.24/3.49/3.72 Ga	$3.51^{+0.019}_{-0.022}$ Ga	3.51 Ga
OP27					$3.39^{+0.088}_{-0.20}$ Ga	3.39 Ga
OP28	2.1 Ga	2.1 Ga	2.56 Ga	2.87 Ga	$3.23^{+0.12}_{-0.28}$ Ga $3.51^{+0.043}_{-0.060}$ Ga	3.30 Ga
OP29	1.2 Ga	1.2 Ga	1.81 Ga	2.10 Ga	$1.17^{+0.25}_{-0.25}$ Ga	1.17 Ga
OP30		3.3 Ga			$3.39^{+0.051}_{-0.075}$ Ga	3.39 Ga
OP31	3.5 Ga	3.5 Ga			$3.33^{+0.081}_{-0.15}$ Ga $3.54^{+0.045}_{-0.064}$ Ga $3.12^{+0.16}_{-0.37}$ Ga $3.48^{+0.032}_{-0.041}$ Ga	3.39 Ga
OP32					$3.09^{+0.12}_{-0.20}$ Ga	3.09 Ga
OP33					$2.71^{+0.40}_{-0.56}$ Ga	2.71 Ga
OP34					$3.30^{+0.098}_{-0.21}$ Ga	3.30 Ga
OP35					$3.60^{+0.042}_{-0.058}$ Ga	3.60 Ga
OP36	2.8 Ga	2.8 Ga	1.79/2.46/3.52 Ga	2.06/2.88/3.49 Ga	$2.04^{+0.15}_{-0.15}$ Ga $2.26^{+0.27}_{-0.28}$ Ga	2.12 Ga
OP37	3.4 Ga	3.4 Ga			$3.30^{+0.039}_{-0.050}$ Ga $3.31^{+0.082}_{-0.15}$ Ga	3.30 Ga
OP38		3.1 Ga			$3.14^{+0.14}_{-0.29}$ Ga $2.91^{+0.22}_{-0.33}$ Ga	2.93 Ga
OP39					$2.94^{+0.17}_{-0.25}$ Ga	2.94 Ga
OP40	3.3 Ga	3.3 Ga			$3.33^{+0.054}_{-0.079}$ Ga $3.37^{+0.033}_{-0.042}$ Ga	3.36 Ga
OP41	2.0 Ga	2.0 Ga	1.71/3.21/3.81 Ga	1.97/3.27/3.80 Ga	$1.71^{+0.29}_{-0.29}$ Ga $1.73^{+0.19}_{-0.19}$ Ga	1.72 Ga
OP42	1.2 Ga	1.2 Ga	1.73 Ga	2.00 Ga	$3.12^{+0.065}_{-0.086}$ Ga $2.92^{+0.17}_{-0.24}$ Ga	3.01 Ga
OP43	1.9 Ga	1.9 Ga	1.84 Ga	2.13 Ga	$2.08^{+0.16}_{-0.16}$ Ga $2.09^{+0.25}_{-0.25}$ Ga	2.08 Ga
OP44		3.3 Ga	1.85 Ga	2.13 Ga	$3.36^{+0.039}_{-0.051}$ Ga $3.27^{+0.065}_{-0.10}$ Ga $3.36^{+0.056}_{-0.083}$ Ga	3.34 Ga
OP45		3.7 Ga			$3.12^{+0.061}_{-0.080}$ Ga $3.02^{+0.14}_{-0.23}$ Ga $3.02^{+0.23}_{-0.51}$ Ga $3.14^{+0.18}_{-0.50}$ Ga	3.10 Ga

Table 1. Cont.

Unit	Hiesinger et al. (2011) [25]	Chen et al. (2022) [51]	Morota et al. (2011) Model A [4]	Morota et al. (2011) Model B [4]	Model Ages in This Study	Mean Model Ages in This Study
OP46	3.3 Ga				$3.65^{+0.045}_{-0.064}$ Ga $3.49^{+0.051}_{-0.077}$ Ga $3.60^{+0.039}_{-0.052}$ Ga	3.59 Ga
OP47	2.1 Ga	2.1 Ga	1.58/3.48 Ga	1.81/3.48 Ga	$1.55^{+0.14}_{-0.14}$ Ga	1.55 Ga
OP48	3.5 Ga	3.5 Ga			$3.29^{+0.038}_{-0.049}$ Ga $3.54^{+0.024}_{-0.028}$ Ga	3.45 Ga
OP49	1.7 Ga	1.7 Ga	1.87/3.70 Ga	2.17/3.69 Ga	$1.67^{+0.080}_{-0.080}$ Ga	1.67 Ga
OP50	3.0 Ga	3.0 Ga	2.60 Ga	2.91 Ga	$3.14^{+0.13}_{-0.26}$ Ga $3.12^{+0.083}_{-0.12}$ Ga $3.38^{+0.038}_{-0.048}$ Ga	3.21 Ga
OP51	3.3 Ga	3.3 Ga			$3.35^{+0.079}_{-0.15}$ Ga $3.24^{+0.081}_{-0.14}$ Ga $3.25^{+0.15}_{-0.52}$ Ga	3.31 Ga
OP52	3.7 Ga				$3.51^{+0.029}_{-0.036}$ Ga $3.34^{+0.090}_{-0.19}$ Ga $3.54^{+0.055}_{-0.086}$ Ga	3.47 Ga
OP53	3.1 Ga	3.1 Ga			$3.28^{+0.062}_{-0.094}$ Ga $3.20^{+0.13}_{-0.29}$ Ga	3.24 Ga
OP54	3.4 Ga	3.4 Ga			$3.25^{+0.091}_{-0.17}$ Ga $3.48^{+0.076}_{-0.15}$ Ga	3.3 Ga
OP55	3.3 Ga	3.3 Ga			$3.05^{+0.26}_{-0.78}$ Ga	3.05 Ga
OP56					$3.34^{+0.16}_{-0.98}$ Ga $3.44^{+0.069}_{-0.12}$ Ga	3.37 Ga
OP57	2.6 Ga	2.6 Ga	2.87 Ga	3.06 Ga	$2.35^{+0.38}_{-0.39}$ Ga $2.22^{+0.38}_{-0.39}$ Ga	2.23 Ga
OP58	3.1 Ga	3.1 Ga			$3.25^{+0.11}_{-0.27}$ Ga	3.25 Ga
OP59	2.1 Ga	2.1 Ga	2.15/3.72 Ga	2.50/3.71 Ga	$2.47^{+0.25}_{-0.26}$ Ga	2.47 Ga
OP60	2.4 Ga	2.4 Ga			$3.42^{+0.096}_{-0.25}$ Ga $3.35^{+0.057}_{-0.087}$ Ga	3.36 Ga
OP61	3.0 Ga	3.0 Ga	2.05 Ga	2.37 Ga	$2.75^{+0.24}_{-0.29}$ Ga	2.75 Ga
OP62	2.6 Ga	2.6 Ga	2.47 Ga	2.79 Ga	$2.33^{+0.27}_{-0.28}$ Ga	2.33 Ga
OP63		3.5 Ga			$3.28^{+0.062}_{-0.094}$ Ga $3.39^{+0.12}_{-0.43}$ Ga $3.45^{+0.069}_{-0.12}$ Ga	3.42 Ga
OP64	1.3 Ga	1.3 Ga	1.73/3.58 Ga	1.99/3.57 Ga	$2.51^{+0.26}_{-0.27}$ Ga $2.44^{+0.42}_{-0.45}$ Ga $2.39^{+0.21}_{-0.22}$ Ga	2.43 Ga

Table 1. Cont.

Unit	Hiesinger et al. (2011) [25]	Chen et al. (2022) [51]	Morota et al. (2011) Model A [4]	Morota et al. (2011) Model B [4]	Model Ages in This Study	Mean Model Ages in This Study
OP65					$3.47^{+0.092}_{-0.24}$ Ga	3.47 Ga
OP66	2.5 Ga	2.5 Ga	1.50/2.99 Ga	1.72/3.15 Ga	$1.38^{+0.17}_{-0.17}$ Ga $1.43^{+0.14}_{-0.14}$ Ga	1.40 Ga
OP67	3.5 Ga	3.5 Ga			$3.20^{+0.077}_{-0.12}$ Ga	3.20 Ga
OP68	2.1 Ga	2.1 Ga			$2.95^{+0.25}_{-0.47}$ Ga $3.09^{+0.21}_{-0.56}$ Ga	2.98 Ga
OP69					$3.46^{+0.043}_{-0.060}$ Ga $3.61^{+0.034}_{-0.044}$ Ga	3.54 Ga
OP70	3.6 Ga	3.6 Ga			$3.57^{+0.034}_{-0.044}$ Ga $3.45^{+0.053}_{-0.080}$ Ga	3.56 Ga
OP71	2.1 Ga	2.1 Ga	1.88 Ga	2.18 Ga	$3.39^{+0.079}_{-0.16}$ Ga $3.53^{+0.095}_{-0.28}$ Ga	3.41 Ga
OP72	3.3 Ga	3.3 Ga			$3.62^{+0.037}_{-0.049}$ Ga $3.51^{+0.039}_{-0.052}$ Ga	3.56 Ga
OP73	3.5 Ga	3.5 Ga			$3.48^{+0.040}_{-0.054}$ Ga $3.37^{+0.080}_{-0.16}$ Ga	3.44 Ga
OP74	3.5 Ga	3.5 Ga			$3.29^{+0.070}_{-0.11}$ Ga	3.29 Ga
OP75	2.1 Ga	2.1 Ga	1.76 Ga	2.04 Ga	$1.89^{+0.28}_{-0.28}$ Ga	1.89 Ga
OP76	2.1 Ga	2.1 Ga	1.88 Ga	2.18 Ga	$1.89^{+0.25}_{-0.25}$ Ga $2.12^{+0.28}_{-0.28}$ Ga	2.05 Ga
OP77	3.4 Ga	3.4 Ga			$3.49^{+0.050}_{-0.074}$ Ga $3.20^{+0.11}_{-0.22}$ Ga $3.38^{+0.066}_{-0.11}$ Ga $3.23^{+0.085}_{-0.15}$ Ga	3.44 Ga
OP78	2.3 Ga	2.3 Ga	1.91 Ga	2.21 Ga	$2.60^{+0.45}_{-0.56}$ Ga	2.60 Ga
OP79	1.7 Ga	1.7 Ga	1.97 Ga	2.28 Ga	$1.79^{+0.19}_{-0.19}$ Ga	1.79 Ga
OP80	3.0 Ga	3.0 Ga	2.73/3.66 Ga	2.98/3.64 Ga	$3.54^{+0.043}_{-0.061}$ Ga $3.44^{+0.055}_{-0.083}$ Ga	3.49 Ga
OP81	3.0 Ga	3.0 Ga	2.73/3.66 Ga	2.98/3.64 Ga	$2.90^{+0.21}_{-0.31}$ Ga $3.17^{+0.13}_{-0.29}$ Ga $3.13^{+0.20}_{-0.59}$ Ga	2.96 Ga
OP82					$3.17^{+0.13}_{-0.29}$ Ga $3.44^{+0.035}_{-0.045}$ Ga	3.17 Ga
OP83	3.3 Ga	3.3 Ga			$3.42^{+0.064}_{-0.11}$ Ga $3.26^{+0.14}_{-0.44}$ Ga $3.32^{+0.091}_{-0.19}$ Ga	3.43 Ga

Table 1. Cont.

Unit	Hiesinger et al. (2011) [25]	Chen et al. (2022) [51]	Morota et al. (2011) Model A [4]	Morota et al. (2011) Model B [4]	Model Ages in This Study	Mean Model Ages in This Study
OP84					$3.52^{+0.081}_{-0.18}$ Ga $3.50^{+0.084}_{-0.19}$ Ga	3.51 Ga
OP85					$3.49^{+0.055}_{-0.085}$ Ga $3.64^{+0.070}_{-0.14}$ Ga	3.59 Ga
OP86	3.7 Ga	3.7 Ga			$2.84^{+0.14}_{-0.16}$ Ga $2.80^{+0.29}_{-0.40}$ Ga	2.83 Ga
OP87	3.1 Ga	3.1 Ga			$2.72^{+0.13}_{-0.14}$ Ga	2.72 Ga
OP88	3.4 Ga	3.4 Ga			$2.39^{+0.36}_{-0.37}$ Ga	2.39 Ga
OP89	3.4 Ga	3.4 Ga			$2.87^{+0.16}_{-0.20}$ Ga	2.87 Ga
OP90	3.4 Ga	3.4 Ga			$2.36^{+0.29}_{-0.30}$ Ga	2.36 Ga
OP91	2.1 Ga	2.1 Ga			$3.41^{+0.064}_{-0.11}$ Ga	3.41 Ga
OP92					$1.93^{+0.40}_{-0.40}$ Ga	1.93 Ga
OP93	2.1 Ga	2.1 Ga	2.19/3.39 Ga	2.49/3.40 Ga	$2.14^{+0.36}_{-0.36}$ Ga	2.14 Ga
OP94	2.1 Ga	2.1 Ga	2.99 Ga	3.12 Ga	$2.91^{+0.23}_{-0.37}$ Ga	2.91 Ga
OP95	3.5 Ga	3.5 Ga			$2.85^{+0.35}_{-0.62}$ Ga	2.85 Ga
OP96	3.5 Ga	3.5 Ga			$2.83^{+0.23}_{-0.32}$ Ga	2.83 Ga
OP97	2.1 Ga	2.1 Ga	1.88 Ga	2.18 Ga	$3.06^{+0.12}_{-0.18}$ Ga $3.14^{+0.15}_{-0.36}$ Ga	3.07 Ga
OP98	3.3 Ga	3.3 Ga			$2.53^{+0.63}_{-0.88}$ Ga $2.33^{+0.24}_{-0.25}$ Ga	2.54 Ga
OP99	3.4 Ga	3.4 Ga			$3.69^{+0.019}_{-0.022}$ Ga	3.69 Ga
OP100	3.4 Ga	3.4 Ga	2.34 Ga	2.74 Ga	$1.98^{+0.20}_{-0.20}$ Ga	1.98 Ga

In this study, using the most recent CSFD data, we found that the model ages of basaltic geological units in the Oceanus Procellarum region range from approximately 3.69 Ga to 1.17 Ga. This implies that lunar basaltic volcanic activity lasted more than 2.5 Ga, further supporting the notion of an extensive duration of basaltic eruptions in the Oceanus Procellarum region.

The CSFD measurements indicate that 51 basaltic units in the Oceanus Procellarum region formed during the late Imbrian epoch. During this period, lunar basaltic eruptions were most extensive. A total of 16 units formed during the early Eratosthenian epoch, while an additional 33 units formed during the late Eratosthenian epoch (Table 1).

In the Oceanus Procellarum region, the youngest mare basalt unit, OP29, dates back to 1.17 Ga, situated in the northwestern part of the Nielsen impact crater (Figure 6a), corresponding to a small region on the northern side of the Aristarchus Plateau. The most ancient mare basalt unit, OP99, traces back to 3.69 Ga, located in the northernmost part of the region (Figure 6b). Concurrently, younger lunar mare basalt units are predominantly distributed in the central area of Oceanus Procellarum, while older basalt units are concentrated along its periphery. Younger lunar mare basalt units primarily occupy the central region of Oceanus Procellarum, while older basalt units are concentrated along its periphery (Table 1). We obtained chronological results from the landing site of the CE-5 mission, corresponding to OP09, yielding an age of 2.06 Ga (Figure 6c). The landing site of Luna 7 is within the

mare basalt unit OP49, with a determined age of 1.67 Ga (Figure 6d). Luna 8's landing site is within the mare basalt unit OP40, and the determined age in the second dating region of this unit is 3.37 Ga (Figure 6e). Luna 13's landing site is within the mare basalt unit OP41, revealing a determined age of 1.73 Ga in the second dating region of this unit (Figure 6f). The determined age of unit OP03 is 3.58 Ga (Figure 6g), OP05 is 2.21 Ga (Figure 6h), and OP21 is 3.36 Ga (Figure 6i).

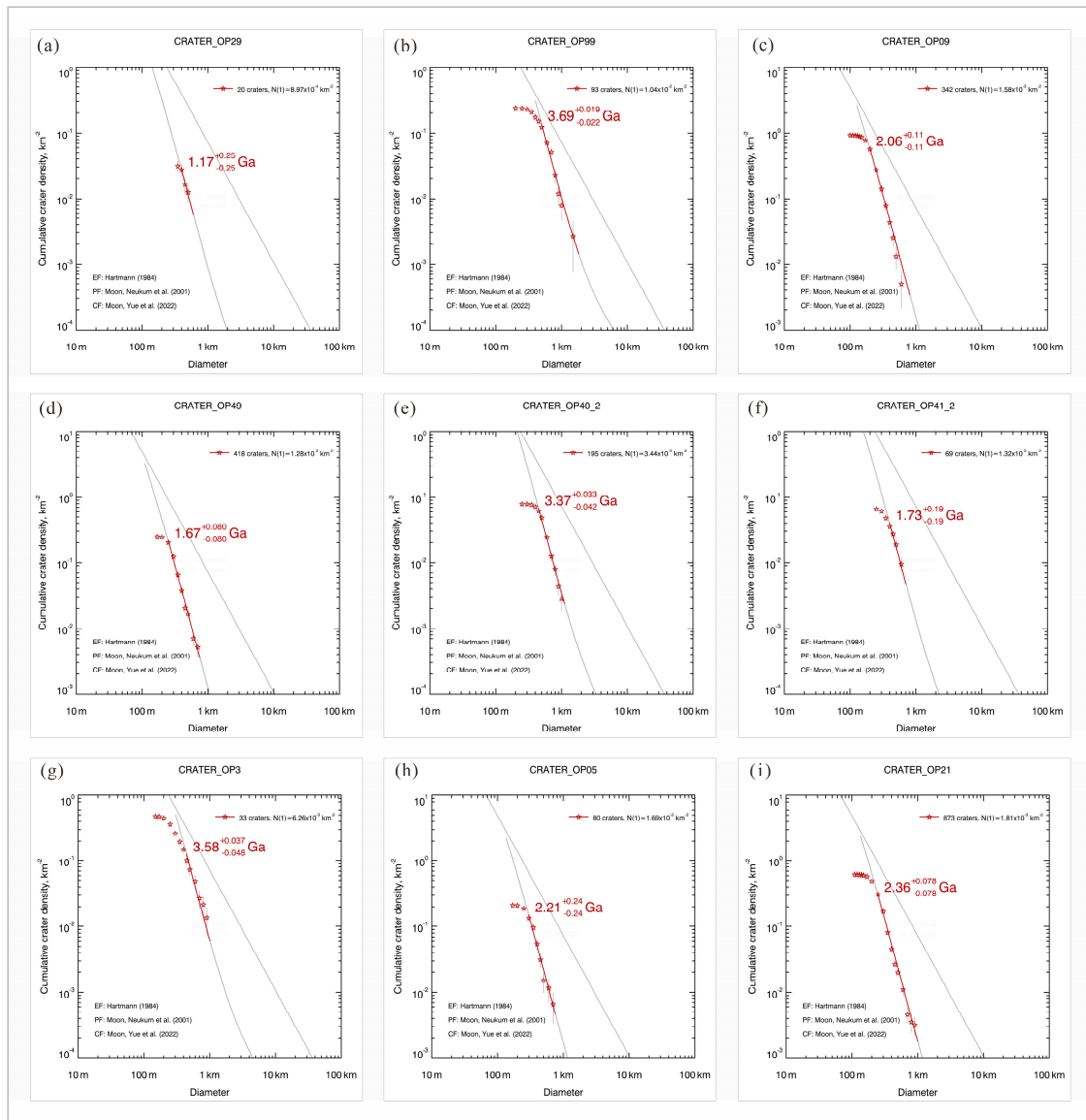


Figure 6. Cumulative crater frequency diagrams and absolute model ages (AMAs) for selected mare basalt units in the Oceanus Procellarum region. Including (EF = ‘Hartmann (1984) [15]’; PF = ‘Moon, Neukum et al. (2001) [47]’; CF = ‘Moon, Yue et al. (2022) [17]’) (a) OP29, the youngest mare basalt unit. (b) OP99, the most ancient mare basalt unit. (c) OP09, the mare basalt unit at the CE-5 landing site. (d) OP49, the mare basalt unit at Luna 7 landing site. (e) OP40, the mare basalt unit at Luna 8 landing site. (f) OP41, the mare basalt unit at Luna 13 landing site. (g) OP03, a mare basalt unit. (h) OP05, a mare basalt unit. (i) OP21, a mare basalt unit.

3.3. Composition of the Oceanus Procellarum Region

According to the Kaguya/SELENE MI false-color composite images, the Oceanus Procellarum region exhibits distinct hues. The northern portion appears orange, denoting a higher iron content, whereas the central and southern areas appear dark blue, signifying a higher titanium content [96]. Notable color variations are observed around the Aristarchus

crater (Figure 6a). Elemental abundance maps reveal elevated FeO and TiO₂ contents in the central and southwestern parts of Oceanus Procellarum compared to those in the northern area. Furthermore, distinct elemental contents are observed in the Kepler and Copernicus craters relative to their surroundings. The northwestern and northern regions of Oceanus Procellarum exhibit higher MgO and Al₂O₃ contents and Mg# values. Additionally, enhanced MgO, Al₂O₃, and Mg# abundances are observed in the Aristarchus, Copernicus, and Kepler craters, as well as some smaller craters, suggesting the excavation of fresh ejecta.

Mineral abundance maps are based on the work of Lemelin et al. (2015; 2019) [62,63], derived from Kaguya Multiband Imager (MI) data. The Kaguya team's topographic correction results within the latitude range of $\pm 50^\circ$ are relatively accurate, focusing primarily on this latitude band for their inversion. Furthermore, this limitation has minimal impact on the mineral analysis of the Oceanus Procellarum region. Mineral abundance maps indicate that the area around the Aristarchus crater within the Oceanus Procellarum region contains the highest olivine content (Figure 7a). Moreover, the orthopyroxene and clinopyroxene contents are comparatively higher in the northwestern part of the Marius crater than in most areas surrounding the Aristarchus crater, implying the significant influence of ejecta from the Aristarchus crater (Figure 7b,c). Generally, the plagioclase content distribution is opposite to that of orthopyroxene and clinopyroxene (Figure 7d).

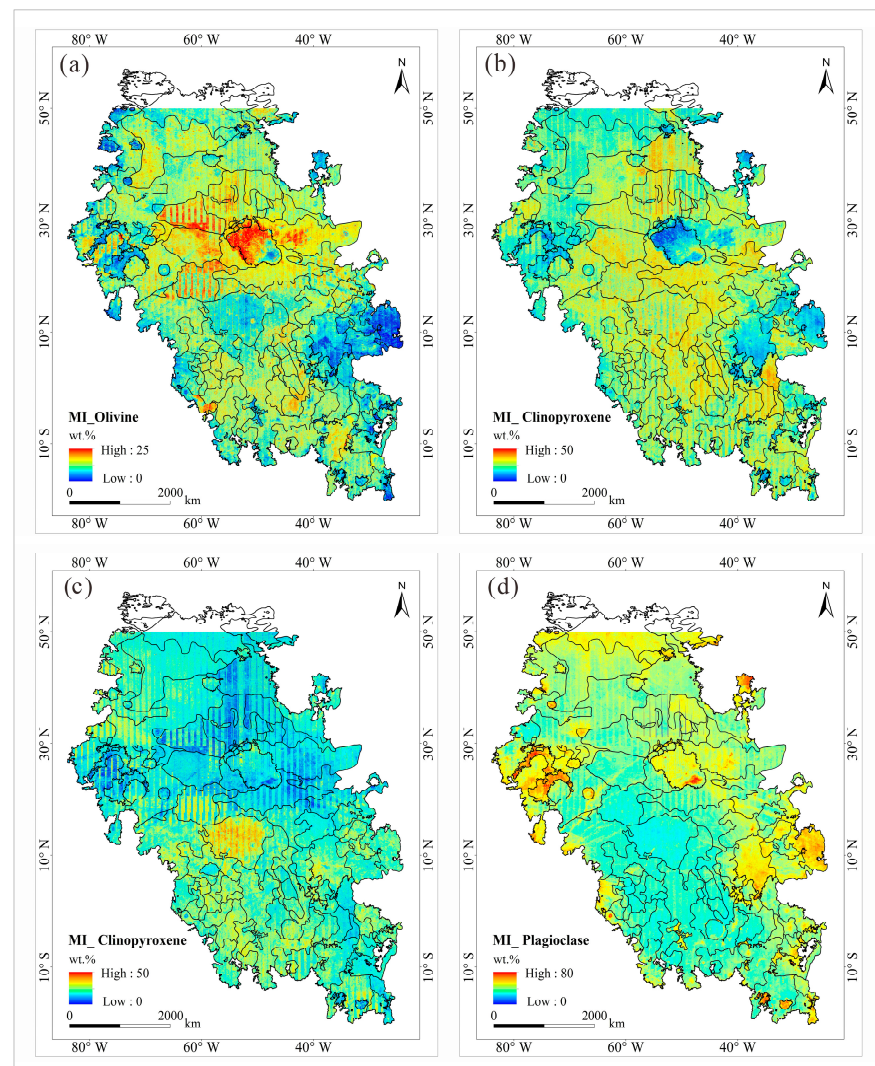


Figure 7. Mineral abundance maps of the Oceanus Procellarum region: (a) olivine, (b) clinopyroxene, (c) orthopyroxene, and (d) plagioclase.

4. Discussion

4.1. Reliability Assessment of Ages Determined by CSFD Method

The CSFD method is widely employed in geology, especially in lunar chronology studies. This method scrutinizes the distribution of impact craters on the lunar surface, offering vital insights into the relative timing of geological events. Hiesinger et al. (2011) [25] partitioned the mare basalt in the Oceanus Procellarum region into 58 units and 68 counting areas. They employed the Neukum chronology model [49] based on Clementine data to determine ages for individual basaltic units (Figure 8a). Subsequently, Morota et al. (2011) [4], Chen et al. (2022) [51], Zhao et al. (2023) [3], and others conducted basaltic unit division and dating studies in specific regions of the Oceanus Procellarum. In this study, the mare basalt in the Oceanus Procellarum region is segmented into 100 units and 167 counting areas, with ages determined for each unit (Figure 8b).

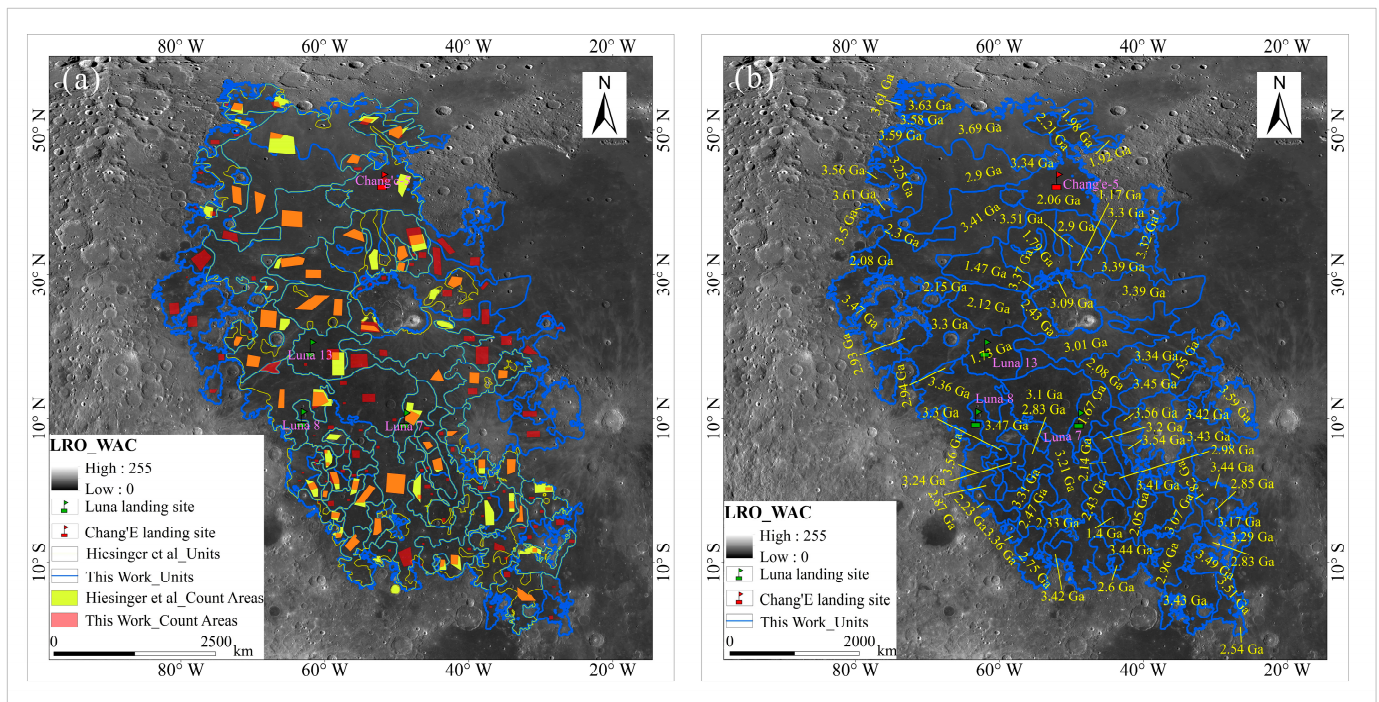


Figure 8. A comparative diagram of mare basalt unit boundaries and counting areas in the Oceanus Procellarum region: this study and Hiesinger et al. (2011) [25] (a), and model ages of basalt units in the Oceanus Procellarum region (b).

This division is characterized by meticulous unit segmentation, extensive partitioning areas, utilization of the latest age model, relatively high image resolution, and typical counting areas. (1) Detailed segmentation of basaltic units can differentiate mare basalt units that erupted at different times but have similar compositions. For example, the determined ages for units OP04 and OP99 are 2.9 Ga and 3.69 Ga, respectively, whereas Hiesinger et al. (2011) [25] grouped them into the same mare basalt unit with an age of 3.4 Ga. OP97 and OP76 units have basalt ages of 3.07 Ga and 2.05 Ga, respectively, but Hiesinger et al. (2011) [25] grouped them into the same mare basalt unit with a determined age of 2.1 Ga. Therefore, detailed unit segmentation enables a more precise distinction of mare basalts with age differences. (2) This basalt dating study identifies previously unextracted and partitioned areas, such as OP84, OP98, OP17, OP46, OP12, OP15, OP18, and OP20, which were overlooked by Hiesinger et al. (2011) [25]. (3) The basalt dating in this study incorporates the age model of Yue et al. (2022) [17], integrating the ages of Chang'e-5 samples, reflecting the model's accuracy. (4) Kaguya/SELENE TC image data and Kaguya/SELENE MI data have high resolutions, providing element maps and false-color images with relatively high resolution. This ensures the integrity and accuracy

of the extracted small impact craters. (5) A total of 167 counting areas were selected, all in flat regions with a lack of secondary impact craters. Multiple counting areas in the same region also ensure the accuracy of age determination results.

In 2023, the isochronous age of China's CE-5 lunar sample landing site was determined to be 2.03 Ga [10–12], challenging previous understandings of lunar chronology. In this study, the chronological results at the CE-5's landing site, corresponding to OP09, brought back an age of 2.06 Ga. This age differs notably from measurements by Hiesinger et al. (2011) [25] but aligns closely with determinations from Morota et al. (2011) [4], Chen et al. (2022) [51], Zhao et al. (2023), and Li et al. (2021) [10–12]. The landing sites of Luna 13, Luna 7, and Luna 8 are located in basaltic units OP49, OP40, and OP41, respectively. The ages determined in this study substantially agree with the results of Hiesinger et al. (2003; 2011) [5,25], Zhao et al. (2023) [3], Morota et al. (2011) [4], and Chen et al. (2022) [51]. The ages of basaltic units OP03, OP05, and OP21 are 3.58 Ga, 2.21 Ga, and 2.36 Ga, respectively, showing significant differences from the dating results of Hiesinger et al. (2011) [25] but aligning closely with Morota et al. (2011) [4]. This further emphasizes the reliability and accuracy of our dating results.

4.2. Geologic Evolution of the Oceanus Procellarum Region

The geomorphological description of the Oceanus Procellarum region is of paramount importance in comprehending the geological evolution of this lunar mare. Within this region, there is a relative abundance of ridges, sinuous rilles, and domal structures compared to other mare areas. These features reflect the region's rich and complex internal dynamic geological processes. It has been observed that the ridges and sinuous rilles primarily align with the NW–SE direction, indicating a substantial influence of compressional stress in the NE–SW direction within the Oceanus Procellarum region. However, further exploration is required to fully comprehend the reasons behind this influence. The region also harbors a significant number of concealed impact craters, with most of these areas being covered by lunar mare basalts. This suggests that their formation predates that of the mare basalts. Additionally, the Oceanus Procellarum region is characterized by an abundance of radial-rayed impact craters and a considerable number of well-preserved impact craters, making it a crucial location for the study of young impact craters. Furthermore, the identification of linear structures through stratigraphic relationships can assist in delineating basaltic units.

Mare basalts are the products of volcanic eruptions on the lunar surface and serve as tangible evidence of the Moon's internal thermal evolution [2]. By examining the eruption events and spatial distribution characteristics of mare basalts, we can indirectly deduce the magnitude, duration, and geological progression of the Moon's internal magmatic activity, either locally or globally. The Oceanus Procellarum region has experienced diverse geological processes, including magma ocean differentiation, crustal plutonic magmatism, volcanic activity, and external meteoroid impact events [3]. CSFD dating results for the Oceanus Procellarum region reveal five major basalt eruption events (Figure 9a). The initial period occurred between 3.69 Ga and 3.14 Ga, when the most extensive eruptions occurred; this eruption encompassed the majority of the Oceanus Procellarum region, with lava flows totaling approximately 1,048,048 km², accounting for approximately 54.2% of the region's area. The mare basalt eruption intensity peaked at approximately 3.42 Ga. The subsequent period commenced from 3.14 Ga to 2.60 Ga, when lava flows were primarily concentrated in three extensive areas, covering approximately 353,664 km² or approximately 18.2% of the region's total area. The third period spanned 2.60 Ga to 2.29 Ga and was characterized by scattered lava flows distributed across seven mare basalt units, covering a combined area of 104,625 km² or approximately 5.4% of the total region. The fourth period emerged from 2.29 Ga to 1.60 Ga, encompassing an area of approximately 343,225 km² or 17.7% of the total region. The final period extended from 1.60 Ga to 1.17 Ga and was primarily distributed across three mare basalt units located on the western side of Kepler crater and on the northeastern and northwestern sides of Aristarchus crater; these units covered an

area of 84,157 km² or approximately 4.4% of the total area. Overall, the mare basalt eruption scale gradually diminished, ultimately ending at approximately 1.17 Ga (Figure 9b,c).

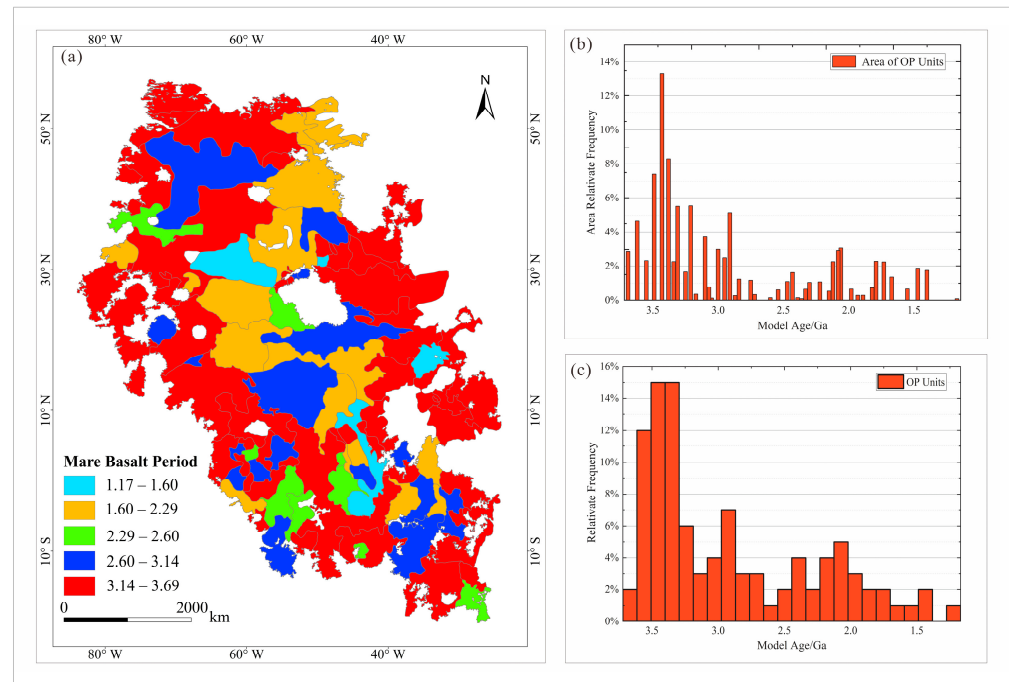


Figure 9. Evolution of mare basalts in the Oceanus Procellarum region. (a) Evolution diagram of mare basalts. Relative frequency and chart of mare basalt epochs showing model ages (b) and areas (c) of mare basalts units in the Oceanus Procellarum region.

4.3. Compositional Variation of Mare Basalts

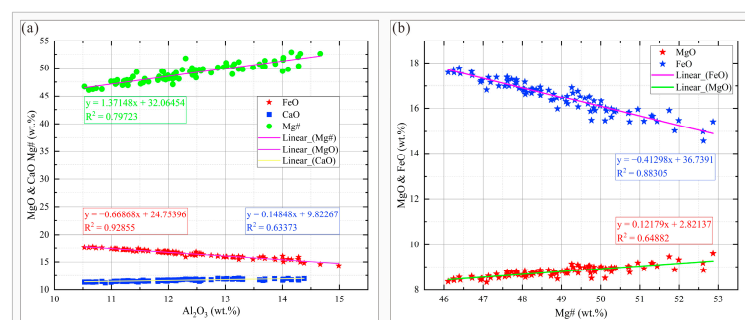
Mare basalt units are characterized by FeO contents exceeding 10 wt.% [45]. The TiO₂ content serves as a crucial discriminator for mare basalt classification, mirroring the fundamental compositional traits of the lunar mantle source region and being closely linked to lunar magma ocean differentiation processes [97]. Based on their TiO₂ content, mare basalts can be further classified into five categories: very-low-titanium (VLT, TiO₂ ≤ 1.5 wt.%), low-titanium (LT, 1.5 wt.% < TiO₂ ≤ 4.5 wt.%), medium-titanium (MT, 4.5 wt.% < TiO₂ ≤ 7.5 wt.%), high-titanium (HT, 7.5 wt.% < TiO₂ ≤ 9.5 wt.%), and very-high-titanium (VHT, TiO₂ > 9.5 wt.%) basalts [98–103]. In the Oceanus Procellarum region, three primary mare basalt types are observed: VLT, LT, and MT. Among these types, LT basalts are the most prevalent, encompassing approximately 49.76% of the total area, followed by VLT basalts at approximately 25.26% and MT basalts making up 24.99% of the total area. These mare basalt types exhibit significant associations with eruption epochs. The first, second, and third epochs predominantly feature VLT, LT, and MT basalt types, respectively, whereas the fourth and fifth epochs primarily feature LT and MT basalt types. Within the first epoch (3.69–3.14 Ga), LT basalts dominate, with minimal MT basalt occurrences. During the second epoch (3.14–2.60 Ga) and the third epoch (2.60–2.29 Ga), MT basalts are prevalent. The fourth epoch (2.29–1.60 Ga) and the fifth epoch (1.60–1.17 Ga) feature mostly MT basalts. Across these epochs, the proportion of MT mare basalts gradually increases from the first to the fifth epoch, whereas the proportion of LT mare basalt decreases. Moreover, the proportion of VLT mare basalt exhibits a consistent decrease over time (Table 2).

Table 2. Elemental and mineral abundance data for mare basalts in the Oceanus Procellarum region.

Model_Age	Al ₂ O ₃ /wt. %	TiO ₂ /wt. %	FeO/wt. %	CaO/wt. %	Mg#	Ol/wt. %	Cpx/wt. %	Opx/wt. %	Pl/wt. %	Type
3.69–3.14 Ga	12.975	2.642	16.031	11.849	50.064	19.889	24.648	17.122	40.872	MT/LT/VLT
3.14–2.60 Ga	12.211	2.812	16.612	11.637	48.534	20.358	25.862	15.936	40.048	MT/LT/VLT
2.60–2.29 Ga	11.626	3.843	16.870	11.574	47.806	20.999	25.939	13.910	39.379	MT/LT/VLT
2.29–1.60 Ga	11.493	4.370	16.798	11.556	47.802	21.148	26.420	13.374	40.865	MT/LT
1.60–1.17 Ga	11.257	5.455	17.261	11.429	47.403	23.547	26.516	11.566	40.224	MT/LT

In the Oceanus Procellarum region, mare basalts of different ages exhibit variations in their composition and mineral content. Specifically, Al₂O₃, CaO, Mg#, orthopyroxene (Opx), and plagioclase (Pl) contents are positively correlated with the ages of mare basalts, while FeO, TiO₂, olivine (Ol), and clinopyroxene (Cpx) contents are directly negatively correlated with age (Table 2). This study unveils an augmented presence of MgO, Al₂O₃, and Mg# in the Aristarchus, Copernicus, and Kepler craters as well as some smaller craters. On the one hand, mare basalts in the Oceanus Procellarum region may undergo the influence of lunar space weathering, characterized by a substantial coverage of loose regolith layers. Fresh impact craters excavate unaltered basalt from the subsurface, resulting in elemental variations between the crater floor and its surroundings. On the other hand, substantial impact events might penetrate the lunar crust, extracting material rich in olivine from deeper layers, leading to significant disparities in MgO, Al₂O₃, and Mg# content.

The lunar magma ocean (LMO) [104] hypothesis postulates that, during the solidification of magma oceans, olivine crystallizes first. Owing to its higher density, olivine tends to descend towards the bottom of the magma ocean during crystallization and differentiation. In contrast, orthopyroxene, with a relatively lower density, may undergo upward movement during differentiation, thereby completing the crust–mantle differentiation on the Moon. Our research findings suggest a slight increase in olivine content with the age of basalt, while orthopyroxene exhibits a slight decrease with basalt age. Consequently, we hypothesize that young lunar basalts in the Oceanus Procellarum region may have originated from partial magma upwelling induced by mantle thermal flux, predominantly emanating from the deep lunar mantle. This outcome aligns with the lunar magma ocean hypothesis. The LMO hypothesis posits that plagioclase and clinopyroxene are pivotal minerals in the lunar highlands. The lunar mantle is enriched in olivine, with aluminum being abundant in orthopyroxene, calcium in anorthite, and magnesium in olivine. Therefore, The Al₂O₃ abundance in mare basalts from the Oceanus Procellarum region is positively correlated with CaO abundance and Mg# but negatively correlated with MgO abundance (Figure 10a). Mg# is directly related to MgO abundance and inversely related to FeO abundance (Figure 10b). Therefore, In the oldest mare basalt units of the Oceanus Procellarum region, the TiO₂, FeO, and olivine contents can reach 0.83 wt.%, 12.99 wt.%, and 17.59 wt.%, respectively. The CaO content reaches 12.84 wt.%. In the youngest mare basalt units, the TiO₂ content can reach 3.69 wt.%, the FeO content can reach 16.93 wt.%, the olivine content can reach 18.39 wt.%, and the CaO content can reach 11.41 wt.%.

**Figure 10.** Mineralogical and elemental analyses of the Oceanus Procellarum region. (a) Correlation of Al₂O₃ abundance with that of other elements. (b) Relationships between Mg# and abundances of other elements.

5. Conclusions

This study comprehensively investigated the morphology, mineralogy, composition, and chronology of mare basalts in the Oceanus Procellarum region. We utilized Kaguya/SELENE TC images, SLDEM2015 data, mineral and chemical compositional maps derived from Kaguya/SELENE MI datasets, and LROC NAC images for our analyses. The main findings are as follows:

- (1) The Oceanus Procellarum region features abundant volcanism-related features of rilles, wrinkle ridges, and volcanic domes, indicating extensive lunar basaltic volcanism in this area. Simultaneously, the Oceanus Procellarum region is influenced by significant compressional stress in the NE–SW direction;
- (2) The mare basalts in the Oceanus Procellarum region were divided into 100 units, and CSFD dating was conducted. The results indicate that volcanic activity in the Oceanus Procellarum region commenced at approximately 3.69 Ga and persisted until 1.17 Ga, spanning a total duration of ~2.5 Ga. The highest mare basalt eruption flux occurred during the late Imbrian period. The region experienced five major episodes of large-scale mare basalt eruptions, which took place during the following time intervals: 3.69 Ga to 3.14 Ga, 3.14 Ga to 2.60 Ga, 2.60 Ga to 2.29 Ga, 2.29 Ga to 1.60 Ga, and 1.60 Ga to 1.17 Ga. The peak volcanic activity for each episode occurred at approximately 3.40 Ga, 2.92 Ga, 2.39 Ga, 2.07 Ga, and 1.43 Ga, respectively;
- (3) The youngest mare basalts in the Oceanus Procellarum region are located within a small unit north of the Aristarchus crater, which is spatially different from the youngest unit in previous studies. This discovery not only provides crucial insights for a comprehensive understanding of lunar geological evolution but also establishes valuable scientific objectives for future exploration missions. It contributes to unraveling the dynamic history and geological processes of the Moon;
- (4) Three main types of mare basalts are present in the Oceanus Procellarum region: VLT, LT, and MT basalts, with LT basalts being the most abundant. The composition and mineral content of mare basalts are strongly correlated with age. Younger mare basalts exhibit characteristics of evolved parental magma with the highest FeO, TiO₂, clinopyroxene, and fayalitic olivine contents, along with the lowest orthopyroxene, plagioclase, Al₂O₃, and CaO abundances and Mg# values. The olivine content is the highest around the Aristarchus crater, while the northwestern part of the Marius crater contains higher concentrations of orthopyroxene and clinopyroxene.

Author Contributions: Conceptualization, C.Z. and J.C. (Jianping Chen); methodology, C.Z.; software, C.Z.; validation, C.Z., Y.P. (Yiwen Pan), X.L., X.H. and K.W.; formal analysis, C.Z.; resources, C.Z. and Y.P. (Yiwen Pan); data curation, C.Z., J.C. (Jian Chen) and X.L.; writing—original draft preparation, C.Z.; writing—review and editing, C.Z., J.C. (Jianping Chen) and S.W.; visualization, C.Z. and J.C. (Jianping Chen); supervision, C.Z., S.W. and Y.P. (Yue Pang); funding acquisition, J.C. (Jianping Chen). All authors have read and agreed to the published version of the manuscript.

Funding: This research was funded by the Geological Survey of China (Grant No. DD20221645).

Data Availability Statement: Data are contained within the article.

Acknowledgments: The authors gratefully acknowledge Jian Chen, Shuangshuang Wu, and Yiwen Pan for their guidance in mineralogy.

Conflicts of Interest: The authors declare no conflicts of interest.

References

1. National Research Council. *The Scientific Context for Exploration of the Moon*; The National Academies Press: Washington, DC, USA, 2007.
2. Head, J.W. Lunar volcanism in space and time. *Rev. Geophys.* **1976**, *14*, 265–300. [[CrossRef](#)]
3. Zhao, Z.; Chen, J.; Ling, Z.; Lu, X.; Li, Z. Chronology, composition, and mineralogy of mare basalts in the junction of Oceanus Procellarum, Mare Imbrium, Mare Insularum, and Mare Vaporum. *Icarus* **2023**, *397*, 115531. [[CrossRef](#)]

4. Morota, T.; Haruyama, J.; Ohtake, M.; Matsunaga, T.; Honda, C.; Yokota, Y.; Kimura, J.; Ogawa, Y.; Hirata, N.; Demura, H.; et al. Timing and characteristics of the latest mare eruption on the Moon. *Earth Planet. Sci. Lett.* **2011**, *302*, 255–266. [[CrossRef](#)]
5. Hiesinger, H.; Head, J.W., III; Wolf, U.; Jaumann, R.; Neukum, G. Ages and stratigraphy of mare basalts in Oceanus Procellarum, Mare Nubium, Mare Cognitum, and Mare Insularum. *J. Geophys. Res. Planets.* **2003**, *108*, 5065. [[CrossRef](#)]
6. Stöffler, D.; Ryder, G.; Ivanov, B.A.; Artemieva, N.A.; Cintala, M.J.; Grieve, R.A.F. Cratering History and Lunar Chronology. *Rev. Mineral. Geochem.* **2006**, *60*, 519–596. [[CrossRef](#)]
7. Nyquist, L.E.; Shih, C.-Y. The isotopic record of lunar volcanism. *Geochim. Cosmochim. Acta* **1992**, *56*, 2213–2234. [[CrossRef](#)]
8. Righter, K.; Canup, R.M. Chronology and Isotopic Constraints on Lunar Evolution. In *Origin of the Earth and Moon*; University of Arizona Press: Tucson, AZ, USA, 2000; pp. 361–396.
9. Basilevsky, A.T.; Neukum, G.; Nyquist, L. The spatial and temporal distribution of lunar mare basalts as deduced from analysis of data for lunar meteorites. *Planet. Space Sci.* **2010**, *58*, 1900–1905. [[CrossRef](#)]
10. Li, Q.-L.; Zhou, Q.; Liu, Y.; Xiao, Z.; Lin, Y.; Li, J.-H.; Ma, H.-X.; Tang, G.-Q.; Guo, S.; Tang, X.; et al. Two-billion-year-old volcanism on the Moon from Chang’e-5 basalts. *Nature* **2021**, *600*, 54–58. [[CrossRef](#)]
11. Hu, S.; He, H.; Ji, J.; Lin, Y.; Hui, H.; Anand, M.; Tartèse, R.; Yan, Y.; Hao, J.; Li, R.; et al. A dry lunar mantle reservoir for young mare basalts of Chang’e-5. *Nature* **2021**, *600*, 49–53. [[CrossRef](#)]
12. Che, X.; Nemchin, A.; Liu, D.; Long, T.; Wang, C.; Norman, M.D.; Joy, K.H.; Tartese, R.; Head, J.; Jolliff, B.; et al. Age and composition of young basalts on the Moon, measured from samples returned by Chang’e-5. *Science* **2021**, *374*, 887–890. [[CrossRef](#)]
13. Hartmann, W.K. Early lunar cratering. *Icarus* **1966**, *5*, 406–418. [[CrossRef](#)]
14. Neukum, G.; Dietzel, H. On the development of the crater population on the moon with time under meteoroid and solar wind bombardment. *Earth Planet. Sci. Lett.* **1971**, *12*, 59–66. [[CrossRef](#)]
15. Hartmann, W.K. Does crater “saturation equilibrium” occur in the solar system? *Icarus* **1984**, *60*, 56–74. [[CrossRef](#)]
16. Hiesinger, H.; van der Bogert, C.H.; Pasckert, J.H.; Funcke, L.; Giacomini, L.; Ostrach, L.R.; Robinson, M.S. How old are young lunar craters? *J. Geophys. Res.* **2012**, *117*, E00H10. [[CrossRef](#)]
17. Yue, Z.; Di, K.; Wan, W.; Liu, Z.; Gou, S.; Liu, B.; Peng, M.; Wang, Y.; Jia, M.; Liu, J.; et al. Updated lunar cratering chronology model with the radiometric age of Chang’e-5 samples. *Nat. Astron.* **2022**, *6*, 541–545. [[CrossRef](#)]
18. Hiesinger, H.; Head, J.W., III; Wolf, U.; Jaumann, R.; Neukum, G. Ages and stratigraphy of lunar mare basalts in Mare Frigoris and other nearside maria based on crater size-frequency distribution measurements. *J. Geophys. Res. Planets.* **2010**, *115*, E03003. [[CrossRef](#)]
19. Hiesinger, H.; Jaumann, R.; Neukum, G.; Head, J.W. Ages of mare basalts on the lunar nearside. *J. Geophys. Res.* **2000**, *105*, 29239–29275. [[CrossRef](#)]
20. Greeley, R.; Kadel, S.D.; Williams, D.A.; Gaddis, L.R.; Head, J.W.; McEwen, A.S.; Murchie, S.L.; Nagel, E.; Neukum, G.; Pieters, C.M.; et al. Galileo imaging observations of lunar maria and related deposits. *J. Geophys. Res.* **1993**, *98*, 17183–17205. [[CrossRef](#)]
21. Morota, T.; Haruyama, J.; Honda, C.; Ohtake, M.; Yokota, Y.; Kimura, J.; Matsunaga, T.; Ogawa, Y.; Hirata, N.; Demura, H.; et al. Mare volcanism in the lunar farside Moscoviense region: Implication for lateral variation in magma production of the Moon. *Geophys. Res. Lett.* **2009**, *36*, L21202. [[CrossRef](#)]
22. Hiesinger, H.; Head, J.W.; Wolf, U.; Jaumann, R.; Neukum, G. New ages for basalts in Mare Fecunditatis based on crater size-frequency measurements. In *Proceedings of the XXXVII Lunar and Planetary Science Conference, Houston, TX, USA, 13–17 March 2006; Volume 1151*.
23. Haruyama, J.; Ohtake, M.; Matsunaga, T.; Morota, T.; Honda, C.; Yokota, Y.; Abe, M.; Ogawa, Y.; Miyamoto, H.; Iwasaki, A.; et al. Long-Lived Volcanism on the Lunar Farside Revealed by SELENE Terrain Camera. *Science* **2009**, *323*, 905–908. [[CrossRef](#)]
24. Braden, S.E.; Stopar, J.D.; Robinson, M.S.; Lawrence, S.J.; van der Bogert, C.H.; Hiesinger, H. Evidence for basaltic volcanism on the Moon within the past 100 million years. *Nat. Geosci.* **2014**, *7*, 787–791. [[CrossRef](#)]
25. Hiesinger, H.; Head, J.W., III; Wolf, U.; Jaumann, R.; Neukum, G. Ages and stratigraphy of lunar mare basalts: A synthesis. In *Recent Advances and Current Research Issues in Lunar Stratigraphy*; Geological Society of America Special Papers; Geological Society of America: Boulder, CO, USA, 2011; pp. 1–51.
26. Lawrence, D.J.; Puetter, R.C.; Elphic, R.C.; Feldman, W.C.; Hagerty, J.J.; Prettyman, T.H.; Spudis, P.D. Global spatial deconvolution of Lunar Prospector Th abundances. *Geophys. Res. Lett.* **2007**, *34*, L03201. [[CrossRef](#)]
27. Jolliff, B.L.; Gillis, J.J.; Haskin, L.A.; Korotev, R.L.; Wieczorek, M.A. Major lunar crustal terranes: Surface expressions and crust-mantle origins. *J. Geophys. Res. Planets* **2000**, *105*, 4197–4216. [[CrossRef](#)]
28. Haskin, L.A.; Gillis, J.J.; Korotev, R.L.; Jolliff, B.L. The materials of the lunar Procellarum KREEP Terrane: A synthesis of data from geomorphological mapping, remote sensing, and sample analyses. *J. Geophys. Res. Planets* **2000**, *105*, 20403–20415. [[CrossRef](#)]
29. Yamashita, N.; Hasebe, N.; Reedy, R.C.; Kobayashi, S.; Karouji, Y.; Hareyama, M.; Shibamura, E.; Kobayashi, M.; Okudaira, O.; D’Uston, C.; et al. Uranium on the Moon: Global distribution and U/Th ratio. *Geophys. Res. Lett.* **2010**, *37*, L10201. [[CrossRef](#)]
30. Lawrence, D.J.; Elphic, R.C.; Feldman, W.C.; Prettyman, T.H.; Gasnault, O.; Maurice, S. Small-area thorium features on the lunar surface. *J. Geophys. Res. Planets.* **2003**, *108*, 5102. [[CrossRef](#)]
31. Wieczorek, M.A.; Neumann, G.A.; Nimmo, F.; Kiefer, W.S.; Taylor, G.J.; Melosh, H.J.; Phillips, R.J.; Solomon, S.C.; Andrews-Hanna, J.C.; Asmar, S.W.; et al. The Crust of the Moon as Seen by GRAIL. *Science* **2013**, *339*, 671–675. [[CrossRef](#)] [[PubMed](#)]

32. Smith, D.E.; Zuber, M.T.; Neumann, G.A.; Lemoine, F.G.; Mazarico, E.; Torrence, M.H.; McGarry, J.F.; Rowlands, D.D.; Head, J.W.; Duxbury, T.H.; et al. Initial observations from the Lunar Orbiter Laser Altimeter (LOLA). *Geophys. Res. Lett.* **2010**, *37*, L18204. [[CrossRef](#)]
33. Joy, K.H.; Crawford, I.A.; Weider, S.Z. Individual lava flow thicknesses in Oceanus Procellarum and Mare Serenitatis determined from Clementine multispectral data. *Icarus* **2010**, *209*, 323–336.
34. Giguere, T.A.; Boyce, J.M.; Gillis-Davis, J.J.; Trang, D.; Stopar, J.D. Lava flow ages in northeastern Oceanus Procellarum: The need for calibrating crater counting procedures. *Icarus* **2021**, *375*, 114838. [[CrossRef](#)]
35. Zhang, J.; Head, J.W.; Liu, J.; Potter, R.W.K. Lunar Procellarum KREEP Terrane (PKT) Stratigraphy and Structure with Depth: Evidence for Significantly Decreased Th Concentrations and Thermal Evolution Consequences. *Remote Sens.* **2023**, *15*, 1861. [[CrossRef](#)]
36. Zhang, X.; Wu, Y.; Ouyang, Z.; Bugiolacchi, R.; Chen, Y.; Zhang, X.; Cai, W.; Xu, A.; Tang, Z. Mineralogical variation of the late stage mare basalts. *J. Geophys. Res. Planets* **2016**, *121*, 2063–2080. [[CrossRef](#)]
37. Pieters, M.I.S.M. Mineralogy of the last lunar basalts: Results from Clementine. *J. Geophys. Res. Planets* **2001**, *106*, 27887–27900.
38. Tian, H.-C.; Wang, H.; Chen, Y.; Yang, W.; Zhou, Q.; Zhang, C.; Lin, H.-L.; Huang, C.; Wu, S.-T.; Jia, L.-H.; et al. Non-KREEP origin for Chang'e-5 basalts in the Procellarum KREEP Terrane. *Nature* **2021**, *600*, 59–63. [[CrossRef](#)] [[PubMed](#)]
39. Cho, Y.; Morota, T.; Haruyama, J.; Yasui, M.; Hirata, N.; Sugita, S. Young mare volcanism in the Orientale region contemporary with the Procellarum KREEP Terrane (PKT) volcanism peak period ~2 billion years ago. *Geophys. Res. Lett.* **2012**, *39*, L11203. [[CrossRef](#)]
40. Nakamura, R.; Yamamoto, S.; Matsunaga, T.; Ishihara, Y.; Morota, T.; Hiroi, T.; Takeda, H.; Ogawa, Y.; Yokota, Y.; Hirata, N.; et al. Compositional evidence for an impact origin of the Moon's Procellarum basin. *Nat. Geosci.* **2012**, *5*, 775–778. [[CrossRef](#)]
41. Mukherjee, S.; Roy, N.; Singh, P.; Singh, D. Characterisation of surface topography and mineralogy of Cardanus and Krafft craters in the western Procellarum region of Moon. *J. Earth Syst. Sci.* **2022**, *131*, 181. [[CrossRef](#)]
42. Boyce, J.M.; Dial, A.L.; Soderblom, L.A. Ages of the lunar nearside light plains and maria. *Lunar Planet. Sci. Conf. Proc.* **1974**, *1*, 11–23.
43. Boyce, J.M. Ages of flow units in the lunar nearside maria based on Lunar Orbiter IV photographs. *Lunar Planet. Sci. Conf. Proc.* **1976**, *3*, 2717–2728.
44. Young, R. The lunar impact flux radiometric age correlation and dating of specific features. *Proc. Lunar Sci. Conf.* **1977**, *8*, 3457–3473.
45. Schultz, P.H.; Spudis, P.D. Beginning and end of lunar mare volcanism. *Nature* **1983**, *302*, 233–236. [[CrossRef](#)]
46. Hiesinger, H.; Head, J.W., III; Wolf, U.; Jaumann, R.; Neukum, G. Lunar mare basalt flow units: Thicknesses determined from crater size-frequency distributions. *Geophys. Res. Lett.* **2002**, *29*, 1248. [[CrossRef](#)]
47. Hiesinger, H.; Head, J.W., III; Wolf, U.; Neukum, G. Lunar Mare Basalts: Mineralogical Variations with Time. In Proceedings of the 32nd Annual Lunar and Planetary Science Conference, Houston, TX, USA, 12–16 March 2001; Volume 1826.
48. Hiesinger, H.; Jaumann, R.; Neukum, G.; Head, J.W. On the relation of age and titanium content of lunar mare basalts. In Proceedings of the XXIX Lunar and Planetary Science Conference, Houston, TX, USA, 16–20 March 1998; Volume 1243.
49. Neukum, G. *Meteorite Bombardment and Dating of Planetary Surfaces*; National Aeronautics and Space Administration: Washington, DC, USA, 1984.
50. Ivanov, B.A.A.N. Size-Frequency Distributions of Planetary Impact Craters and Asteroids. In *Collisional Processes in the Solar System*; Marov, M.Y., Rickman, H., Eds.; Springer: Dordrecht, The Netherlands, 2001; pp. 1–34.
51. Chen, J.; Ling, Z.; Liu, J.; Chen, S.; Ding, X.; Chen, J.; Cheng, W.; Li, B.; Zhang, J.; Sun, L.; et al. Digital and global lithologic mapping of the Moon at a 1:2,500,000 scale. *Sci. Bull.* **2022**, *67*, 2050–2054. [[CrossRef](#)] [[PubMed](#)]
52. Chisenga, C.; Yan, J.; Zhao, J.; Atekwana, E.A.; Steffen, R. Density Structure of the Rümker Region in the Northern Oceanus Procellarum: Implications for Lunar Volcanism and Landing Site Selection for the Chang'E-5 Mission. *J. Geophys. Res. Planets* **2020**, *125*, e2019JE005978. [[CrossRef](#)]
53. Qian, Y.Q.; Xiao, L.; Zhao, S.Y.; Zhao, J.N.; Huang, J.; Flahaut, J.; Martinot, M.; Head, J.W.; Hiesinger, H.; Wang, G.X. Geology and Scientific Significance of the Rümker Region in Northern Oceanus Procellarum: China's Chang'E-5 Landing Region. *J. Geophys. Res. Planets* **2018**, *123*, 1407–1430. [[CrossRef](#)]
54. Yue, Z.; Di, K.; Liu, Z.; Michael, G.; Jia, M.; Xin, X.; Liu, B.; Peng, M.; Liu, J. Lunar regolith thickness deduced from concentric craters in the CE-5 landing area. *Icarus* **2019**, *329*, 46–54. [[CrossRef](#)]
55. Wu, B.; Huang, J.; Li, Y.; Wang, Y.; Peng, J. Rock Abundance and Crater Density in the Candidate Chang'E-5 Landing Region on the Moon. *J. Geophys. Res. Planets* **2018**, *123*, 3256–3272. [[CrossRef](#)]
56. Zhao, J.; Xiao, L.; Qiao, L.; Glotch, T.D.; Huang, Q. The Mons Rümker volcanic complex of the Moon: A candidate landing site for the Chang'E-5 mission. *J. Geophys. Res. Planets* **2017**, *122*, 1419–1442. [[CrossRef](#)]
57. Xie, M.; Xiao, Z.; Zhang, X.; Xu, A. The Provenance of Regolith at the Chang'e-5 Candidate Landing Region. *J. Geophys. Res. Planets* **2020**, *125*, e2019JE006112. [[CrossRef](#)]
58. Barker, M.; Mazarico, E.; Neumann, G.; Zuber, M.; Haruyama, J.; Smith, D. A new lunar digital elevation model from the Lunar Orbiter Laser Altimeter and SELENE Terrain Camera. *Icarus* **2015**, *273*, 346–355. [[CrossRef](#)]
59. Haruyama, J.; Matsunaga, T.; Ohtake, M.; Morota, T.; Honda, C.; Yokota, Y.; Torii, M.; Ogawa, Y. Global lunar-surface mapping experiment using the Lunar imager/spectrometer on SELENE. *Earth Planets Space* **2008**, *60*, 243–255. [[CrossRef](#)]

60. Robinson, M.S.; Brylow, S.M.; Tschimmel, M.; Humm, D.; Lawrence, S.J.; Thomas, P.C.; Denevi, B.W.; Bowman-Cisneros, E.; Zerr, J.; Ravine, M.A.; et al. Lunar Reconnaissance Orbiter Camera (LROC) Instrument Overview. *Space Sci. Rev.* **2010**, *150*, 81–124. [[CrossRef](#)]
61. Ohtake, M.; Matsunaga, T.; Yokota, Y.; Yamamoto, S.; Ogawa, Y.; Morota, T.; Honda, C.; Haruyama, J.; Kitazato, K.; Takeda, H.; et al. Deriving the Absolute Reflectance of Lunar Surface Using SELENE (Kaguya) Multiband Imager Data. *Space Sci. Rev.* **2010**, *154*, 57–77. [[CrossRef](#)]
62. Lemelin, M.; Lucey, P.G.; Song, E.; Taylor, G.J. Lunar central peak mineralogy and iron content using the Kaguya Multiband Imager: Reassessment of the compositional structure of the lunar crust. *J. Geophys. Res. Planets* **2015**, *120*, 869–887. [[CrossRef](#)]
63. Lemelin, M.; Lucey, P.G.; Miljković, K.; Gaddis, L.R.; Hare, T.; Ohtake, M. The compositions of the lunar crust and upper mantle: Spectral analysis of the inner rings of lunar impact basins. *Planet. Space Sci.* **2019**, *165*, 230–243. [[CrossRef](#)]
64. Otake, H.; Ohtake, M.; Hirata, N. Lunar Iron and Titanium Abundance Algorithms Based on SELENE (Kaguya) Multiband Imager Data. In Proceedings of the 43rd Lunar and Planetary Science Conference, Woodlands, TX, USA, 19–23 March 2012; Volume 1905.
65. Lucey, P.G.; Blewett, D.T.; Hawke, B.R. Mapping the FeO and TiO₂ content of the lunar surface with multispectral imagery. *J. Geophys. Res. Planets.* **1998**, *103*, 3679–3699. [[CrossRef](#)]
66. Wang, X.; Zhang, J.; Ren, H. Lunar surface chemistry observed by the KAGUYA multiband imager. *Planet. Space Sci.* **2021**, *209*, 105360. [[CrossRef](#)]
67. Neukum, G.; Ivanov, B.; Hartmann, W. Cratering Records in the Inner Solar System in Relation to the Lunar Reference System. *Space Sci. Rev.* **2001**, *96*, 55–86. [[CrossRef](#)]
68. Michael, G.G.; Neukum, G. Planetary surface dating from crater size-frequency distribution measurements: Partial resurfacing events and statistical age uncertainty. *Earth Planet. Sci. Lett.* **2010**, *294*, 223–229. [[CrossRef](#)]
69. Michael, G.G. Planetary surface dating from crater size-frequency distribution measurements: Multiple resurfacing episodes and differential isochron fitting. *Icarus* **2013**, *226*, 885–890. [[CrossRef](#)]
70. Pieters, C.M.; Staid, M.I.; Fischer, E.M.; Tompkins, S.; He, G. A Sharper View of Impact Craters from Clementine Data. *Science* **1994**, *266*, 1844–1848. [[CrossRef](#)]
71. Zanetti, M.; Stadermann, A.; Jolliff, B.; Hiesinger, H.; van der Bogert, C.; Plescia, J. Evidence for self-secondary cratering of Copernican-age continuous ejecta deposits on the Moon. *Icarus* **2017**, *298*, 64–77. [[CrossRef](#)]
72. Lu, X.; Cao, H.; Ling, Z.; Fu, X.; Qiao, L.; Chen, J. Geomorphology, Mineralogy, and Geochronology of Mare Basalts and Non-Mare Materials around the Lunar Crisium Basin. *Remote Sens.* **2021**, *13*, 4828. [[CrossRef](#)]
73. Neukum, G.; Koenig, B. Dating of individual lunar craters. *Lunar Planet. Sci. Conf. Proc.* **1976**, *3*, 2867–2881.
74. Hartmann, W.K. Relative crater production rates on planets. *Icarus* **1977**, *31*, 260–276. [[CrossRef](#)]
75. Kneissl, T.; van Gasselt, S.; Neukum, G. Map-projection-independent crater size-frequency determination in GIS environments—New software tool for ArcGIS. *Planet. Space Sci.* **2011**, *59*, 1243–1254. [[CrossRef](#)]
76. Mustard, J.F.; Pieters, C.M.; Isaacson, P.J.; Head, J.W.; Besse, S.; Clark, R.N.; Klima, R.L.; Petro, N.E.; Staid, M.I.; Sunshine, J.M.; et al. Compositional diversity and geologic insights of the Aristarchus crater from Moon Mineralogy Mapper data. *J. Geophys. Res. Planets* **2011**, *116*, E00G12. [[CrossRef](#)]
77. Lucey, P.G.; Hawke, B.R.; Pieters, C.M.; Head, J.W.; McCord, T.B. A compositional study of the Aristarchus Region of the Moon using near-infrared reflectance spectroscopy. *J. Geophys. Res. Solid Earth* **1986**, *91*, 344–354. [[CrossRef](#)]
78. Watters, T.R. Lunar Wrinkle Ridges and the Evolution of the Nearside Lithosphere. *J. Geophys. Res. Planets* **2022**, *127*, e2021JE007058. [[CrossRef](#)]
79. Fryer, R. Moon morphology, interpretations based on lunar orbiter photography. *Earth-Sci. Rev.* **1977**, *13*, 219. [[CrossRef](#)]
80. Solomon, A.M.F.J. Tectonics of mascon loading: Resolution of the strike-slip faulting paradox. *J. Geophys. Res. Planets* **2001**, *106*, 20603–20620.
81. Sharp, V.L.; Head, J.W.I. Lunar mare ridges—Analysis of ridge-crater intersections and implications for the tectonic origin of mare ridges. In Proceedings of the 18th Lunar and Planetary Science Conference, Houston, TX, USA, 16–20 March 1987; pp. 307–317.
82. Strom, R.G. Lunar Mare Ridges, Rings and Volcanic Ring Complexes. *Int. Astron. Union* **1972**, *47*, 187–215. [[CrossRef](#)]
83. Watters, T.R. Wrinkle ridge assemblages on the terrestrial planets. *J. Geophys. Res.-Solid Earth Planets* **1988**, *93*, 10236–10254. [[CrossRef](#)]
84. Yue, Z.; Michael, G.; Di, K.; Liu, J. Global survey of lunar wrinkle ridge formation times. *Earth Planet. Sci. Lett.* **2017**, *477*, 14–20. [[CrossRef](#)]
85. Kochemasov, G.G. Lunar Tectonics. *Encycl. Lunar Sci.* **2018**, 1–4.
86. Nypaver, C.; Thomson, B. New Observations of Recently Active Wrinkle Ridges in the Lunar Mare: Implications for the Timing and Origin of Lunar Tectonics. *Geophys. Res. Lett.* **2022**, *49*, e2022GL098975. [[CrossRef](#)]
87. Yue, Z.; Li, W.; Di, K.; Liu, Z.; Liu, J. Global mapping and analysis of lunar wrinkle ridges. *J. Geophys. Res. Planets* **2015**, *120*, 978–994. [[CrossRef](#)]
88. Head, J.W.; Wilson, L. Generation, ascent and eruption of magma on the Moon: New insights into source depths, magma supply, intrusions and effusive/explosive eruptions (Part 2: Predicted emplacement processes and observations). *Icarus* **2017**, *283*, 176–223. [[CrossRef](#)]

89. Wilson, L.; Head, J.W. Ascent and eruption of basaltic magma on the Earth and Moon. *J. Geophys. Res. Solid Earth* **1981**, *86*, 2971–3001. [[CrossRef](#)]
90. Hurwitz, D.M.; Head, J.W.; Wilson, L.; Hiesinger, H. Origin of lunar sinuous rilles: Modeling effects of gravity, surface slope, and lava composition on erosion rates during the formation of Rima Prinz. *J. Geophys. Res. Planets* **2012**, *117*, E00H14. [[CrossRef](#)]
91. Qian, Y.; Xiao, L.; Head, J.W.; Wilson, L. The Long Sinuous Rille System in Northern Oceanus Procellarum and Its Relation to the Chang'e-5 Returned Samples. *Geophys. Res. Lett.* **2021**, *48*, e2021GL092663. [[CrossRef](#)]
92. Head, J.W.; Gifford, A. Lunar mare domes: Classification and modes of origin. *Earth Moon Planets* **1980**, *22*, 235–258. [[CrossRef](#)]
93. Smith, E.I. Identification, distribution and significance of lunar volcanic domes. *Earth Moon Planets* **1973**, *6*, 3–31. [[CrossRef](#)]
94. Campbell, B.A.; Hawke, B.R.; Campbell, D.B. Surface morphology of domes in the Marius Hills and Mons Rümker regions of the Moon from Earth-based radar data. *J. Geophys. Res. Planets* **2009**, *114*, E01001. [[CrossRef](#)]
95. Whitford-Stark, J.L.; Head, J.W. The Procellarum volcanic complexes: Contrasting styles of volcanism. In Proceedings of the 8th Lunar Science Conference, Houston, TX, USA, 14–18 March 1977; pp. 1008–1010.
96. Qian, Y.; Xiao, L.; Head, J.W.; van der Bogert, C.H.; Hiesinger, H.; Wilson, L. Young lunar mare basalts in the Chang'e-5 sample return region, northern Oceanus Procellarum. *Earth Planet. Sci. Lett.* **2021**, *555*, 116702. [[CrossRef](#)]
97. Neal, C.R.; Taylor, L.A. Petrogenesis of mare basalts: A record of lunar volcanism. *Geochim. Cosmochim. Acta* **1992**, *56*, 2177–2211. [[CrossRef](#)]
98. Charette, M.P.; McCord, T.B.; Pieters, C.; Adams, J.B. Application of remote spectral reflectance measurements to lunar geology classification and determination of titanium content of lunar soils. *J. Geophys. Res.* **1974**, *79*, 1605–1613. [[CrossRef](#)]
99. Pieters, C.M.; Head, J.W.; Sunshine, J.M.; Fischer, E.M.; Murchie, S.L.; Belton, M.; McEwen, A.; Gaddis, L.; Greeley, R.; Neukum, G.; et al. Crustal Diversity of the Moon: Compositional Analyses of Galileo Solid State Imaging Data. *J. Geophys. Res. Part E: Planets* **1993**, *98*, 17127–17148. [[CrossRef](#)]
100. Davis, P.A., Jr. Iron and titanium distribution on the moon from orbital gamma ray spectrometry with implications for crustal evolutionary models. *J. Geophys. Res. Part B: Solid Earth* **1980**, *85*, 3209–3224. [[CrossRef](#)]
101. Sato, H.; Robinson, M.; Lawrence, S.J.; Denevi, B.W.; Hapke, B.; Jolliff, B.L.; Hiesinger, H. Lunar mare TiO₂ abundances estimated from UV/Vis reflectance. *Icarus* **2017**, *296*, 216–238. [[CrossRef](#)]
102. Melendrez, D.E.; Johnson, J.R.; Larson, S.M.; Singer, R.B. Remote sensing of potential lunar resources: 2. High spatial resolution mapping of spectral reflectance ratios and implications for nearside mare TiO₂ content. *J. Geophys. Res.: Planets* **1994**, *99*, 5601–5619. [[CrossRef](#)]
103. Giguere, T.A.; Taylor, G.J.; Hawke, B.R.; Lucey, P.G. The titanium contents of lunar mare basalts. *Meteorit. Planet. Sci.* **2000**, *35*, 193–200. [[CrossRef](#)]
104. Snyder, G.A.; Taylor, L.A.; Neal, C.R. A chemical model for generating the sources of mare basalts: Combined equilibrium and fractional crystallization of the lunar magmasphere. *Geochim. Cosmochim. Acta* **1992**, *56*, 3809–3823. [[CrossRef](#)]

Disclaimer/Publisher's Note: The statements, opinions and data contained in all publications are solely those of the individual author(s) and contributor(s) and not of MDPI and/or the editor(s). MDPI and/or the editor(s) disclaim responsibility for any injury to people or property resulting from any ideas, methods, instructions or products referred to in the content.